Probabilistic Analysis of Compression System Stability Using Importance Sampling

by

Nayden Dimitrov Kambouchev

Submitted to the Department of Aeronautics and Astronautics
in partial fulfillment of the requirements for the degree of

Master of Science

at the

MASSACHUSETTS INSTITUTE OF TECHNOLOGY

February 2005

Author .....
Department of Aeronautics and Astronautics
December 25, 2004

Certified by .....
David Darmofal
Associate Professor of Aeronautics and Astronautics
Thesis Supervisor

Certified by .....
Edward Greitzer
H. N. Slater Professor of Aeronautics and Astronautics
Thesis Supervisor

Accepted by .....
Jaime Peraire
Professor of Aeronautics and Astronautics
Chairman, Department Committee on Graduate Students

Probabilistic Analysis of Compression System Stability Using Importance Sampling

by

Nayden Dimitrov Kambouchev

Submitted to the Department of Aeronautics and Astronautics
on December 25, 2004, in partial fulfillment of the
requirements for the degree of
Master of Science

Abstract

The probability of instability is computed via a new approach based on Importance Sampling and a dynamic compression system model. In contrast to ordinary Monte Carlo methods Importance Sampling offers reduced confidence intervals, reduced number of samples and reduced model execution times. The new approach avoids some of the problematic details associated with the traditional stability margin methodology including the additivity, linearity and normality assumptions. It also captures successfully the phase interaction effects between inlet distortion and stationary asymmetric tip clearance. The phase interaction is an example of a case when the stability margin approach fails to capture both the quantitative and qualitative behaviors.

Thesis Supervisor: David Darmofal
Title: Associate Professor of Aeronautics and Astronautics

Thesis Supervisor: Edward Greitzer
Title: H. N. Slater Professor of Aeronautics and Astronautics

Acknowledgments

First and most importantly, I want to thank all my 16.07 Dynamics students. Without them the last four months of this work would have been a disaster.

Second, I need to thank the following individuals for their help, support and ideas: Juan Castiella, Pierre Dakel, Prof. David Darmofal, Prof. Edward Greitzer, Dr. Tom Hynes of Cambridge University, Justin Jaworski, Kelly Klima, Prof. Paul Lagace, Vai-Man Lei, Sean Nolan, Prof. Jaime Peraire, Robin Riedel, Kiril Sakaliyski, Dr. Borislav Sirakov, Prof. Zoltan Spakovszky, Dr. William Steenken of GE Aircraft Engines, Olivier Toupet and Prof. Karen Willcox. Special thanks to the people from the Robust Engine Group and the teaching fellows of 2004-2005.

The author wishes to gratefully acknowledge the following financial supports without which this work would have not been possible:

- Fellowship from the Department of Aeronautics and Astronautics for the academic year 2003-2004
- H. N. Slater Professorship support during the summer of 2004
- Teaching Fellowship from the Department of Aeronautics and Astronautics for the Fall of 2004.

The original of this section somehow got damaged in the editing process and below is the hexadecimal content of whatever was left of it. A quick Importance Sampling simulation shows that the probability of recovering of the original content is so small that it is not numerically representable in the contemporary computers.

```
EC06 0997 010C 8C0E 090F D2D0 8C0F 0B0D F884 A90C D8DD 0AA4 09DA D006
03AE BC02 000D AF82 080A 8E00 080A 83CB EF08 030F 05DC CC09 B8CB 9DD4
9B01 8A01 D0CE 0D80 0ED8 D4A3 F79D 0B09 0EB0 94FA B4E7 000C 0601 8AF1
8901 0D02 8603 86C4 0BB7 C787 0E05 F508 0E0B 0FDB 89D7 0A00 0EBE 0405
040E B5B0 0106 0108 040A 0704 93E0 EFE5 0FA6 0A00 0C0E 00B1 EC01 03A2
EA00 BED7 F5B0 0E07 0704 0400 0EBE 01A1 08E4 9B03 0A05 BCFE 869D 8DA4
04A5 F790 0B03 07ED 08B5 DF07 089A 0F0C 03B4 020C 0DB3 A600 0DB1 0402
8886 8806 00CE 0BCA CBDA 028A 890F DF0B 06F6 8BF8 0EC0 04F6 01B3 05DF
E8FF D60F 94ED 0800 060C 95EF 0B05 0A0D 05F3 80BD C702 D60A 8906 E60B
```

```
099D 0AB8 07B7 000E 0CCC 0ADD 018D 080B 01B7 0A09 B8F7 0A82 0B09 98FC
0607 AD01 0309 0BF6 00E1 9E06 B3DB 0191 0685 0A09 0C05 0C03 BA0D 0303
0C09 91AA 0DE1 8400 07C9 FD8D D30D 0B09 87F1 0707 D20B 0E0C C80B 979B
00F5 8CEA 0F06 0F09 0E8D 92B4 07FB CDF0 0605 800C 8C05 FDE0 059A 860B
C3E3 00CE A4DB B501 DDA1 CDE4 0082 8E04 B6D0 DF04 C78C 0903 0703 E20F
0504 0F07 95B9 8B89 F409 079B 0AB2 E7A9 0184 BF02 0084 0BE2 B8BD A584
FF02 FA07 E9D9 A60A D4C4 0DAF EB91 D004 E399 0D0F FDBC 090B 958D B7A2
0DF1 C409 FFD5 97DD 0F0C D805 940A 07D5 0DF6 090A 00C3 06AB 0402 0BD5
058D 0D09 0B04 0A0B 01C8 0B00 0784 030C 0606 E18B 89B4 00D1 0802 8EC3
9808 C29D 0088 0E00 0085 0EFB 0B03 C202 0708 CE08 0FB2 A40C 9407 D7BD
FBBD 01C5 0F8C 0307 0799 0AC5 EFC7 A192 F583 088D AD00 C506 F90A DA0C
020A 0900 EC0E B808 0707 D607 F3D8 98D6 FC0D 0F0D 0A03 03F9 8F00 8908
0303 0EC3 0C08 92A7 D2A2 0403 0708 0902 0806 CFBC A1B6 0BCA 0007 A007
0B01 BC02 93DB F702 0A0E D303 FB0B AB04 0707 01B8 8F06 A60E E90C C103
0A0A 0D9E 0882 0EA5 F781 0BC7 A6A4 0DC9 0807 03D9 0092 EFF5 040A E099
0B93 C80D 0EC6 098A B99F 0AD4 9F04 0507 070F 040D 0202 01A8 E902 0EC7
0B87 B592 0FCD E098 F0E3 0009 00ED C99A 050C 8F0E 0093 C689 030A 04BB
05A7 0F0F E009 9BD0 D900 0603 A60B 0A8B 0602 0C95 BBEB 8B0A E704 EFCA
B209 0208 0985 080F F2E6 9E95 D306 070D 810A DFC3 F303 E202 BCAF 04D4
800B BB0E 0A02 D297 010C A005 0AC3 0108 0606 0A02 BAC4 0DC4 0003 0BBC
0502 D6A2 0EA6 0709 0EC3 B5B9 07AE 0BD6 DD9D 960D 00F1 0101 0E0D 8A06
02BA D680 08D9 ACA9 0D09 0C03 8C01 D1CA 0FC5 000B FF84 FDC0 A5FE BA05
0ECA 00F2 0100 03CC 09ED 820A CFDB 0EE2 06D4 C8E6 86F1 04E3 ED0B 0E95
0109 040B F5F3 D000 02C7 E207 F70E 06FD 0BD8 0B92 0102 D7A5 0F06 AD04
050D 88AD 0FB4 FF0F 0407 069D A0D6 0D0D DFBA 0194 0801 9F08 B1FA 0DF1
0EB5 0982 010B 09AF CEA4 B207 CD0F 080A FFEB 940E 9506 05A9 BE0A BA96
0594 0E0F C9BF 07C2 D301 090C 0E0A 05D7 A2F5 0F07 EA09 0208 E9C7 EEEC
030B E801 07F4 B907 0204 8FDF 070C EC0F 04E0 8300 0D0E 09CE EC9F 080E
08CE 0403 D10E 9FC2 02E3 0C0C 0ADE 0A8F C806 0506 0503 BF0D 028B 0101
0C03 CF05 88F8 BF00 060E 0502 0BCD 05F2 C9A4 0F9C 0E04 A704 0AC2 0006
0100 B3BB FD0C 93E1 82D7 A302
```

Nomenclature

Roman

a	scaling factor or speed of sound
b_x	axial chord
B	Greitzer's parameter
c	translation constant
$E[X]$	expected value of the random variable X
E	throttle setting coefficient
$f(x)$	probability density function
$f^*(x)$	probability density function of the modified distribution
i	$\sqrt{-1}$
$I(X)$	the indicator function
l_c	nondimensional compressor length
$\dot{m}_{corr}$	corrected mass-flow
n	wheel speed fraction or harmonic number
p	pressure
p_i	probability of instability
$\hat{p}_i$	estimator of p_i
r	mean wheel radius
T	temperature
U	mean wheel speed
$var(X)$	variance of the random variable X

Greek

α	phase angle between inlet distortion and tip clearance asymmetry
γ	stagger angle
Γ	deterioration rate
ϕ	mass-flow coefficient
ψ	pressure rise
π	pressure ratio
ρ	density
$\lambda,\ \mu$	parameters of the Hynes-Greitzer model
$\sigma,\ \mu$	standard deviation and mean value
θ	circumferential angle
$\omega,\ \tilde{\omega}$	dimensional and nondimentional system eigenvalue

Abbreviations

aSM	available Stability Margin
ID	Inlet Distortion
IS	Importance Sampling
MC	(ordinary) Monte Carlo
MPR	Maximum Pressure Rise
PDF	Probability Density Function
RE	Relative Error
rSM	required Stability Margin
SM	Stability Margin
TC	Tip Clearance
TI	Time Invariant
TV	Time Variant

Contents

List of Figures

List of Tables

Chapter 1

Introduction

1.1 Background

Several types of instabilities can be encountered during aircraft jet engine operation. Some, such as surge and rotating stall, are purely fluid dynamic, some such as flutter arise as result of fluid-structure interaction. This work is concerned only with the former.

Surge is a large amplitude oscillation of the flow through the compressor. It can be accompanied by visible flames from the front and the back of the engine, blade bending and severe engine damage. Rotating stall consists of one or several sectors of reduced or reversed flow with the pattern rotating around the engine circumference. Rotating stall can lead to fatigue damage or loss of thrust, but its more important role is that it is generally a precursor of surge. Both, surge and rotating stall represent limits to operation and there is a great incentive in reducing their occurrences.

1.2 Previous Work

There is a large amount of literature on surge and rotating stall and we only discuss work which is relevant to the present study. The first paper in the open literature on the topic belongs to Emmons et al. [2] who in 1955 provided an explanation of the mechanism by which the reduced flow region travels along the compressor circum-

ference and gave physical insight into surge by showing that the behavior is similar to that of a Helmholtz resonator. Later, in 1976, Greitzer [3] provided a nonlinear model for surge. A theory of rotating stall, based on a traveling wave decomposition, was created by Moore [4] in 1984. Two years later a unified model including both surge and rotating stall was published jointly by Moore and Greitzer [5]. This unified model is the first one to theoretically justify the interaction between the two instability phenomena. Numerical solutions of the model equations in the presence of inlet distortion were obtained by Hynes and Greitzer [6]. Their advancement is due to the use of Fourier spectral methods which emerged as a major computational tool in that time period. The ability to compute the stability numerically via eigenvalue decompositions has stimulated the extension of these models to other problems. Bonnaure extended the stability model to compressible flow [7] allowing for analysis of high speed machines. Graf modified it to quantify the effect of stationary asymmetric tip clearance [1] and Gordon looked at the instability behavior caused by rotating tip clearance asymmetries and radial distortions [8]. The model has also been used for control applications, more notably moving inlet guide vanes have been used by van Schalkwyk and Haynes to design controllers capable of extending the stable flow range of low speed axial compressor subjected to inlet distortion [9, 10]. An extensive summary of most recent developments in the control applications of the models can be found in [11].

All the works described represent deterministic investigations, but there is an increased interest in applying probabilistic techniques into the area of jet engine design. Garzon probabilistically analyzed the impact of geometric variability due to manufacturing on compressor performance quantifying the mean and variation of loss and turning [12, 13]. He showed that the deterministic (i.e. nominal) loss was lower than the mean loss, and that the differences between deterministic and achieved mean compressor efficiency could be as much as 1% at the compressor level. Analysis of the compressor repeating-stage model was performed separately by Lavainne and Vincent [14, 15], who also found that the achieved mean compressor efficiency and pressure rise are worse than the respective deterministically predicted values.

1.3 Objectives and Structure

The objectives of this thesis are:

- Determine questions related to jet engine stability which can be solved by applications of probabilistic techniques, exemplify possible approaches and identify their areas of applicability, advantages and disadvantages.
- Define shortcomings in the commonly used stability margin techniques.

The structure of this thesis is as follows:

- In Chapter 2 the technique of Importance Sampling is applied to the problem of compression system stability in cases without and with aging. A large set of example results is obtained.
- Chapter 3 focuses on the shortcomings of the commonly used stability margin definition. Examples of specific types of problems which may occur are given.
- Chapter 4 describes the coupling effect between inlet distortion and circumferential tip clearance. The coupling is used as an example in which the probabilistic techniques are applied in the assessment of stability.

1.4 Contributions

A new framework for estimation of probabilistic quantities related to jet engine instabilities has been developed. The framework is based on a first principles physical model combined with probabilistic estimation techniques. The outputs of interest include, but are not limited to the probability of instability, mean number of cycles to instability, probability of instability before a given number of cycles, mean number of cycles between instabilities in a fleet.

The main contributions of this thesis are:

- Integration of a dynamic compression system stability model into a probabilistic simulation based on importance sampling and showing that an effective

technique capable of estimating probabilities spanning a wide range of orders of magnitude is *required* because small probability estimation using ordinary Monte Carlo simulations demands a large computational effort.

- For the first time in open literature the probability of instability and several related quantities are calculated from a physically relevant *dynamic* model. A dynamic model is required because static stability is a necessary, but not sufficient for dynamic stability.

- Comparison of the new approach to more traditional estimation methods based on stability margin. Identification of limitations of stability margin techniques and description of cases when erroneous results could be obtained due to these traditional techniques.

- Quantification of the effect of deterioration on the probability of instability. As aircraft engines age, deterioration becomes a significant contributor to the surge events.

- Quantification of the interaction between inlet distortion and asymmetric tip clearance, and demonstration that the relative phase can impact the stability in a substantive manner.

Chapter 2

Probabilistic Methodology

For a jet engine fleet the expected number of instabilities is equal to the probability of instability of a single engine times the size of the fleet. One figure of merit for stability is thus the probability of instability for a single engine.

2.1 Importance Sampling

The probability of instability p_i is a small number, usually less than 1×10^{-4} for commercially certified engines. The event of interest here thus happens very rarely and when standard Monte Carlo (MC) sampling techniques are used to simulate engine behavior many samples are required. There are more efficient simulation techniques for low probability events, Importance Sampling (IS) being one of them. IS increases the confidence in the estimates by sampling from modified distributions, which allows the event of interest to occur more often. Due to the use of modified sampling distributions, the resulting probability must be adjusted appropriately at the end of the simulation.

The estimation of the probability of instability p_i in this work is accomplished by combining Importance Sampling with a dynamic compression system model. The output of the dynamic model is binary – the system is either stable or unstable. The inputs to the dynamic model are provided by the IS algorithm and the resulting probability is weighted based on the IS input distributions.

2.1.1 Description

The Monte Carlo method requires a large number of samples to achieve reasonable confidence (99%) in the estimates of small probabilities. An illustration of this can be created following [16]. Let $\hat{p_i}$ be the MC estimator of the probability of instability p_i given by:

$$\hat{p_i} = \frac{\text{number of instabilities}}{\text{total number of samples}} \tag{2.1}$$

The variance of this estimator is

$$var(\hat{p_i}) = \frac{p_i - p_i^2}{\text{total number of samples}} \approx \frac{p_i}{\text{total number of samples}}, \tag{2.2}$$

for small p_i ($p_i \leq 1 \times 10^{-2}$). The estimated 99% confidence interval for p_i is $[\hat{p_i} - 3\sqrt{var(\hat{p_i})},\ \hat{p_i} + 3\sqrt{var(\hat{p_i})}]$. To guarantee an error less than 20%, the following condition must be satisfied:

$$3\sqrt{var(\hat{p_i})} < 0.20\ p_i, \tag{2.3}$$

which is equivalent to

$$\text{total number of samples} > \frac{225}{p_i}. \tag{2.4}$$

If $p_i = 1{\times}10^{-4}$ the required number of samples is larger than $2{\times}10^6$ and if $p_i = 1{\times}10^{-6}$ it is larger than $2{\times}10^8$. These are prohibitive numbers for any Monte Carlo simulation that relies on a realistic and therefore, computationally expensive dynamic model.

One possible approach is to simplify the dynamic model until its execution time is small enough to allow taking the required large number of samples, but this decreases the model fidelity. Another approach is to use Importance Sampling, reducing the required number of samples and keeping the full dynamic model.

If the indicator function I is defined as

$$I(X) = \begin{cases} 1 & \text{if X represents a stable system} \\ 0 & \text{if X represents an unstable system} \end{cases}, \tag{2.5}$$

the probability p_i can be rewritten as

$$p_i = E[I(X)] = \int I(x)f(x)dx = \int I(x)\frac{f(x)}{f^*(x)}f^*(x)dx = E^*[I(X)\frac{f(X)}{f^*(X)}], \quad (2.6)$$

where $f(x)$ is the probability density function (PDF) of the random variable X and $f^*(x)$ is another probability density function such that $f(x) = 0$ whenever $f^*(x) = 0$. Equation (2.6) suggests the following estimator for p_i:

$$\hat{p_i} = \frac{\sum I(X)\frac{f(X)}{f^*(X)}}{\text{total number of samples}} \quad (2.7)$$

The variance of this estimator is

$$var^*(\hat{p_i}) = \frac{E[I(X)\frac{f(X)}{f^*(X)}] - p_i^2}{\text{total number of samples}} \quad (2.8)$$

For an appropriately chosen function $f^*(x)$, the variance given by (2.8) will be less than the variance given by (2.2) leading to a reduction in the required number of samples for a given confidence interval. An inappropriate choice of $f^*(X)$, however, can greatly increase the required number of samples [17], so Importance Sampling must be applied with caution.

The optimal $f^*(X)$ which gives the best possible performance requires the knowledge of the value of p_i and therefore is not known, but choices for $f^*(X)$, which give good confidence bounds, do exist. The two most common ones are Importance Sampling via scaling and Importance Sampling via translation. In IS via scaling the new PDF $f^*(x)$ is defined as

$$f^*(x) = \frac{1}{a}f(\frac{x}{a}), \quad (2.9)$$

and in IS via translation it is defined as

$$f^*(x) = f(x - c), \quad (2.10)$$

where $a > 1$ and $c > 0$. Examples of a scaled and a translated normal distribution are shown in Figure 2-1.

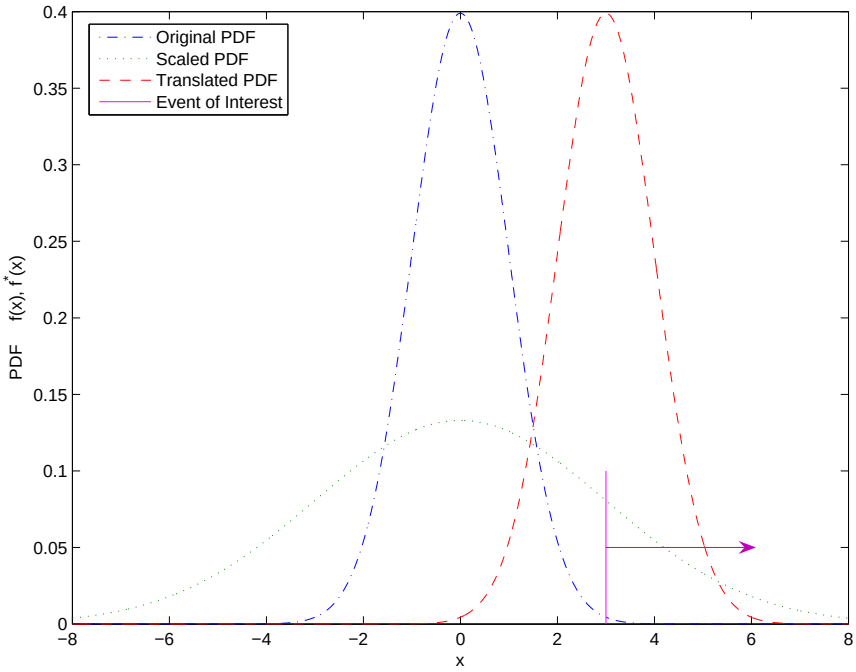

Figure 2-1: Scaled ($a = 3$) and translated ($c = 3$) probability density functions for use in Importance Sampling.

2.1.2 Performance Assessment of Importance Sampling

There is no "ready to use" recipe how to choose the parameters a and c. To gain insight into the Importance Sampling process, and to determine general guidelines for the parameters, a series of tests with a normal distribution were performed. Each test simulation has a single random input X that is distributed according to a standard normal distribution with zero mean and standard deviation equal to one. The observed event of interest A is defined as

$$A = \{x > x_{limit}\}, \tag{2.11}$$

where x_{limit} is a preselected constant. For each test, 1000 random samples of X are taken and the probability p_A of A is estimated using IS. The estimate $\hat{p}_A$ is compared to the real probability p_A, which can be computed analytically for this simple event type.

Figure 2-2 displays the predictions $\hat{p}_A$, obtained with Importance Sampling via

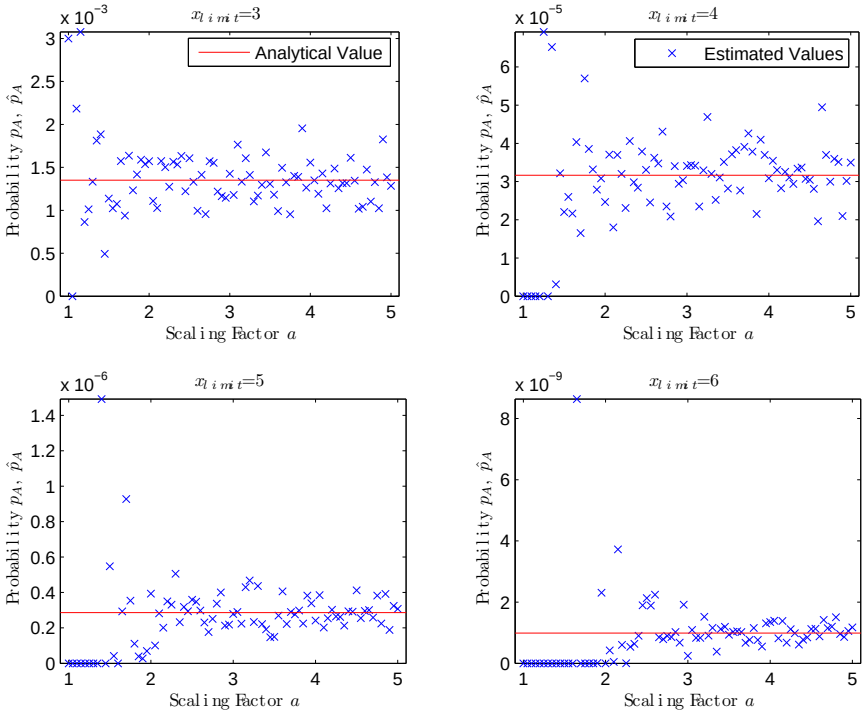

Figure 2-2: Importance Sampling via scaling applied to four small probability events A. Small scaling factors, which include Monte Carlo ($a = 1$), fail to provide meaningful non-zero estimates as the probability of the event decreases.

scaling for four different values of x_{limit}. As the probability of the event decreases, scaling factors close to 1 ($a = 1$ is the Monte Carlo method) do not provide an estimate different than zero (no instabilities are recorded for any of the thousand samples). For the range of low probability events considered, scaling $a = 3$ is found to be optimal in the sense that it is enough to guarantee non-zero prediction with 1000 samples when the probability of interest is within $[1 \times 10^{-9},\ 1 \times 10^{-3}]$. Unless otherwise stated, a equals 3 in all simulation results presented later in this work; all predictions fall into the range of probabilities displayed by the four plots in Figure 2-2.

The use of $a = 3$ also provides good 99% confidence bounds on the estimate as shown in Figure 2-3. It is typical for Importance Sampling confidence bounds to decrease sharply with the initial increase of the scaling factor and then flatten out [16, 17]. Even though not visible from the figure, it can be shown that there is no further benefit of increasing the scaling factor [16].

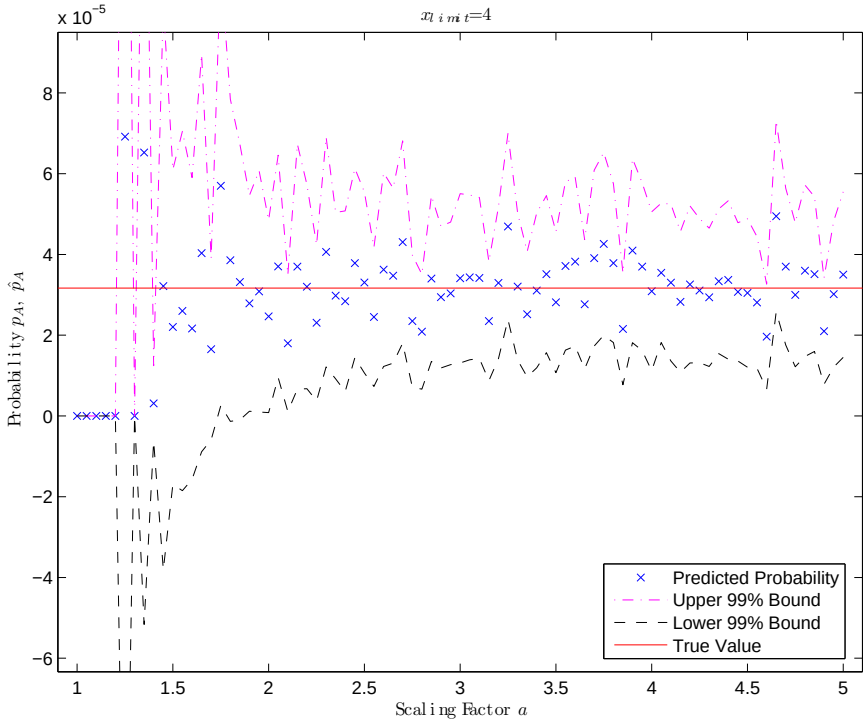

Figure 2-3: The typical behavior of the lower and upper 99% estimated confidence bounds for Importance Sampling via scaling (1000 samples) consists of a sharp initial decrease and a flat follow-up section.

The results for Importance Sampling via translation are given in Figure 2-4. Small amounts of translation as well as large ones should be avoided because they lead to estimate $\hat{p}_A = 0$ because no events occurred during the simulation. Again there is a relatively flat region in which the predicted value is not sensitive to the amount of translation. Based on the expected probability ranges for the simulations, the default translation amount is chosen to be equal to four standard deviations (the input distribution is a normal one with standard deviation equal to one).

From a comparison of Figures 2-5 and 2-3 Importance Sampling via translation is seen to provide better 99% confidence intervals. This is not surprising because, as Figure 2-1 shows, translation moves more of the weight of the probability density function into the region of interest, while scaling tends also to move probabilistic weight into regions in which the event A does not occur (in this case to the left of zero).

The results presented above assume normal input distributions and the simple

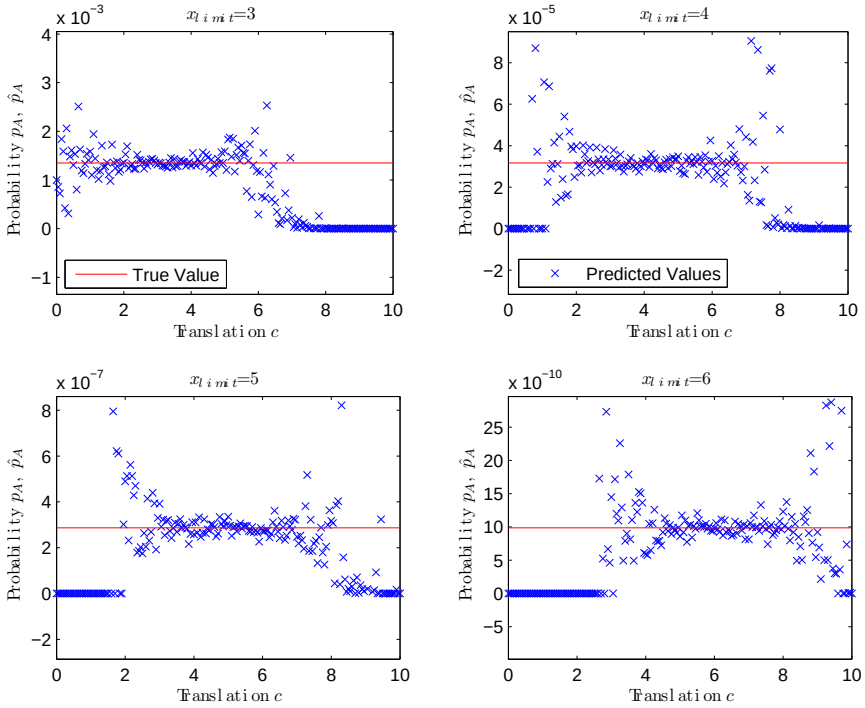

Figure 2-4: Importance Sampling via translation is applied to four small probability events. Small and large translation numbers factors which include Monte Carlo ($c = 0$) fail to provide meaningful non-zero estimates as the probability of the event decreases.

event A. For less idealized situations, the benefits of both Importance Sampling methods can be expected to be less because of nonlinearities in the definition of A. It is especially important for the definition of A to be "monotonic" for scaling and translation to work. For translation this implies that as the input x goes from $-\infty$ to $+\infty$ there should be at most one value of x where a switch from not being in A to being in A occurs. For scaling there should be at most two such switching positions. Table 2.1 compares Importance Sampling versus Monte Carlo simulations for the probability of instability of a compression system for three different cases (the details of the compression system model are given in Section 2.2). For the baseline case, Monte Carlo gives a large 99% confidence interval, which even includes negative numbers. Comparing the three simulation runs for case B_1 even when the number of samples is increased 10 times, the confidence interval of Monte Carlo remains worse than the confidence interval of IS. The advantage of Importance Sampling is more apparent in cases B_2 and B_3 which correspond to a 3% reduction in the throttle setting

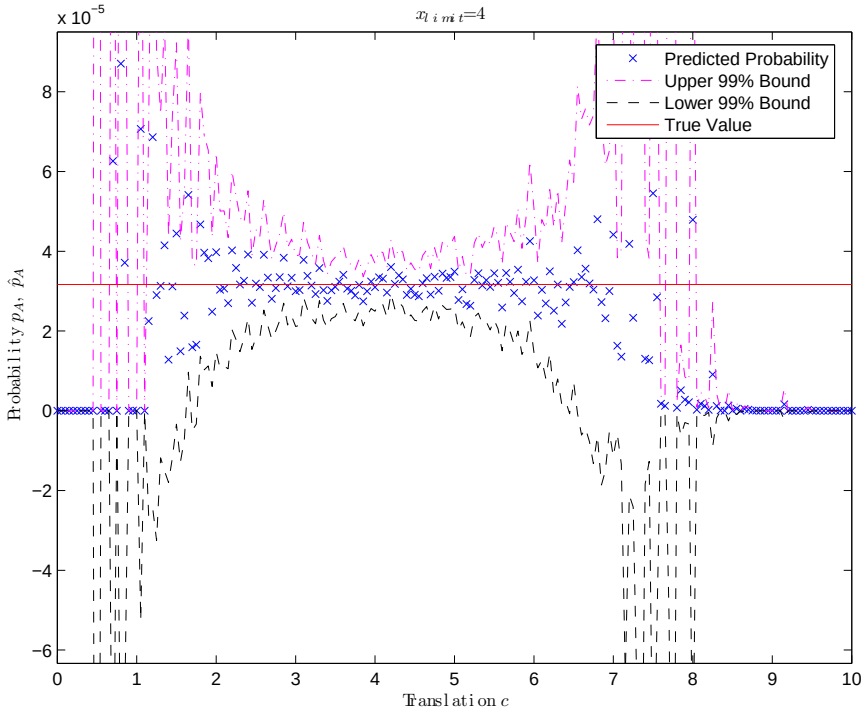

Figure 2-5: The typical behavior of the lower and upper 99% estimated confidence bounds for Importance Sampling via translation (1000 samples) consists of a sharp initial decrease, a flat follow-up section, and a sharp blow-up.

relative to B_1 (or in other words, moving away from the unstable configurations) and 50% reduction in the variability of the inputs relative to B_1 respectively. Monte Carlo fails to obtain non-zero estimates of the probability of instability while IS gives reasonable values, even though the confidence intervals are worse than those for case B_1.

2.2 Dynamic Compression System Model

The compression system model used in this thesis is the incompressible Hynes-Greitzer model [6] and its extension by Graf that includes nonuniform stationary tip clearance [1]. Relative to the IS procedure, the model is a black box, so it could be replaced with a compressible model [7] or models including radial distortions and rotating tip clearances [8] without any conceptual modifications.

The jet engine is modeled as consisting of an inlet, a compressor, a large plenum

Table 2.1: Performance comparison of Monte Carlo and Importance Sampling for compression system stability

Test Case	Algorithm	Samples	Upper Bound	Probability $\hat{p}_i$	Lower Bound
B_1	MC	1000	1.33×10^{-2}	0.60×10^{-2}	-0.13×10^{-2}
B_1	IS	1000	0.51×10^{-2}	0.38×10^{-2}	$+0.25 \times 10^{-2}$
B_1	MC	10000	0.66×10^{-2}	0.46×10^{-2}	$+0.25 \times 10^{-2}$
B_2	MC	1000	$0.00 \times 10^{+0}$	$0.00 \times 10^{+0}$	$+0.00 \times 10^{+0}$
B_2	IS	1000	4.23×10^{-4}	2.44×10^{-4}	$+0.65 \times 10^{-4}$
B_3	MC	1000	$0.00 \times 10^{+0}$	$0.00 \times 10^{+0}$	$+0.00 \times 10^{+0}$
B_3	IS	1000	5.67×10^{-6}	1.42×10^{-6}	-2.83×10^{-6}

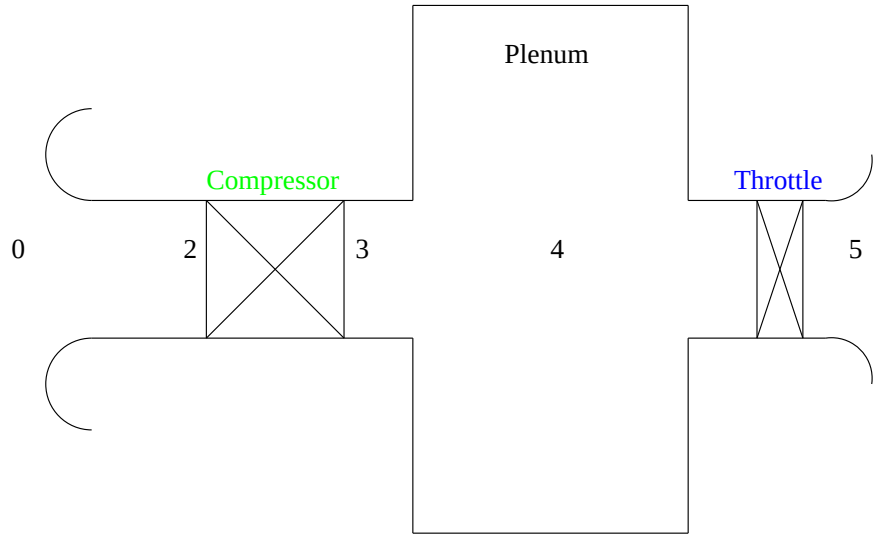

Figure 2-6: Compression system schematic for the Hynes-Greitzer model

behind the compressor and a throttle. Figure 2-6 shows a schematic of the configuration. The fluid is assumed incompressible everywhere with the exception of the plenum where it behaves as a gas spring. The compressor is assumed to behave as an actuator disc over which the pressure rise ψ occurs. The pressure rise ψ is defined as

$$\psi = \frac{p_3 - p_{t2}}{\rho U^2}, \tag{2.12}$$

where p_3 is the compressor exit static pressure, p_{t2} is the compressor inlet total pressure, ρ is the fluid density and U is the wheel speed at the mean radius. The pressure rise characteristic has a maximum in the region of interest while the throttle pressure drop has a parabolic dependence on the specific massflow ϕ as shown in Figure 2-7.

The throttle pressure drop is defined as

$$\psi = E\phi^2, \tag{2.13}$$

where E is the throttle coefficient and $\phi = \frac{v}{U}$ is the specific massflow (v is the axial velocity of the flow). Depending on the throttle setting E, the compression system

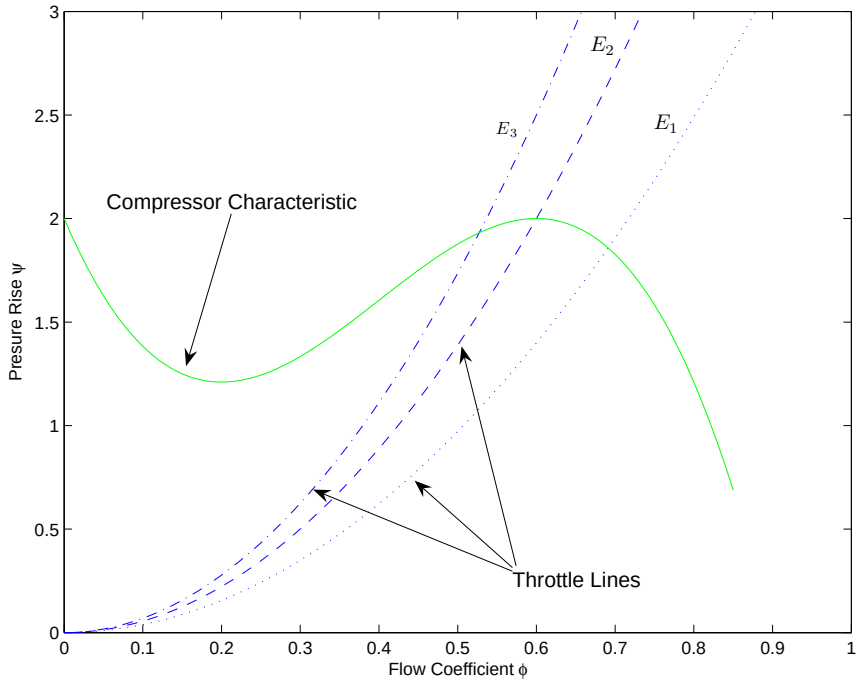

Figure 2-7: Compressor and throttle characteristics – throttle characteristic E_1 has a stable operating point, characteristic E_2 has a marginally stable operating point and characteristic E_3 has an unstable operating point

operating point (the intersection of the compressor and throttle characteristics) is either in a stable, or in an unstable region.

The stability boundary of the model in axisymmetric flow is the peak of the compressor characteristic [4, 5]. For throttle characteristics to the right of characteristic E_2 (such as E_1), the operation is stable and small disturbances decay; for throttle characteristics to the left of characteristic E_2 (such as E_3), the operation is unstable and small disturbances grow until the nonlinearities in the compressor characteristic become important and a limit cycle (surge) forms [4].

To find the growth rates of the different modes representing the small circumfer-

ential disturbances a solution procedure based on Fourier spectral decomposition is used. The presence of an eigenvalue with positive real parts implies growth of the system mode with time and therefore instability. The detailed equations of the model can be found in Appendix D.

In asymmetric cases involving variable tip clearance or inlet distortion, the effective compressor pressure rise curve (the overall system curve) retains the general shape shown in Figure 2-7, but the peak is usually a little lower and the instability limit is not the peak itself, but some point to the right of it.

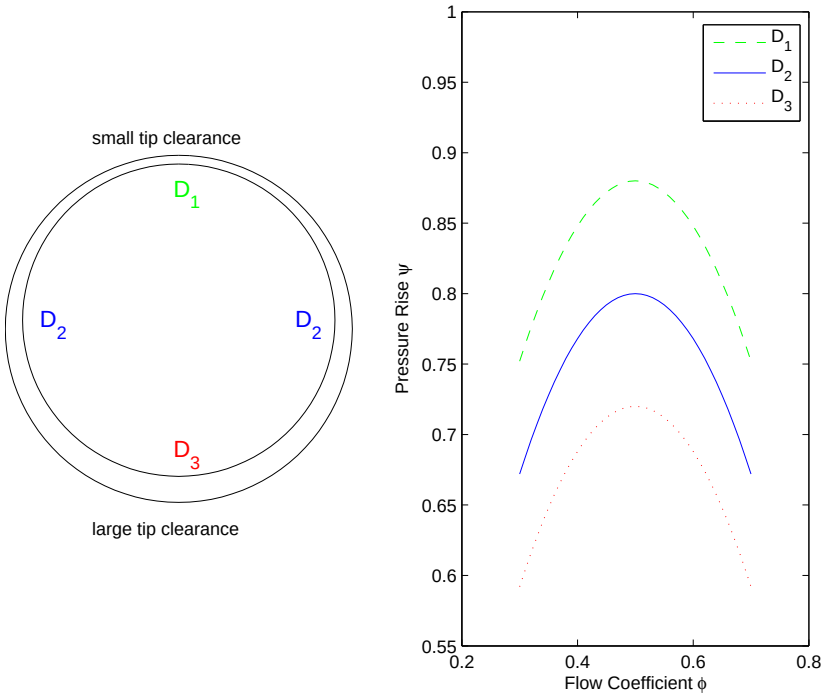

Figure 2-8: Asymmetric tip clearance geometry and its effect on the local compressor pressure rise characteristic (following Graf [1])

The computational model was adapted by Graf [1] to predict the stability of a compression system with asymmetric stationary tip clearance in the compressor. His approach assumes that increasing the tip clearance reduces the pressure rise [18]. Therefore for a compressor with a rotor as shown in Figure 2-8, different points on the circumference have different pressure rises. Point D_1 represents a region with small tip clearance and therefore higher than nominal pressure rise (point D_2). Point D_3 represents a region with increased tip clearance and therefore pressure rise lower

than at point D_2. Each point on the circumference has its own local pressure rise characteristic and the combination of all local pressure rise characteristics determines the overall system stability. The numerical simulations performed by Graf and the experimental data obtained by Wong [19] showed that in general the presence of asymmetry tends to reduce the overall stability as compared to an axisymmetric case.

2.3 Probabilistic Instability Simulations

A simplified data flow chart between the Importance Sampling procedure and the dynamic model described in the previous section is shown in Figure 2-9. The inputs to

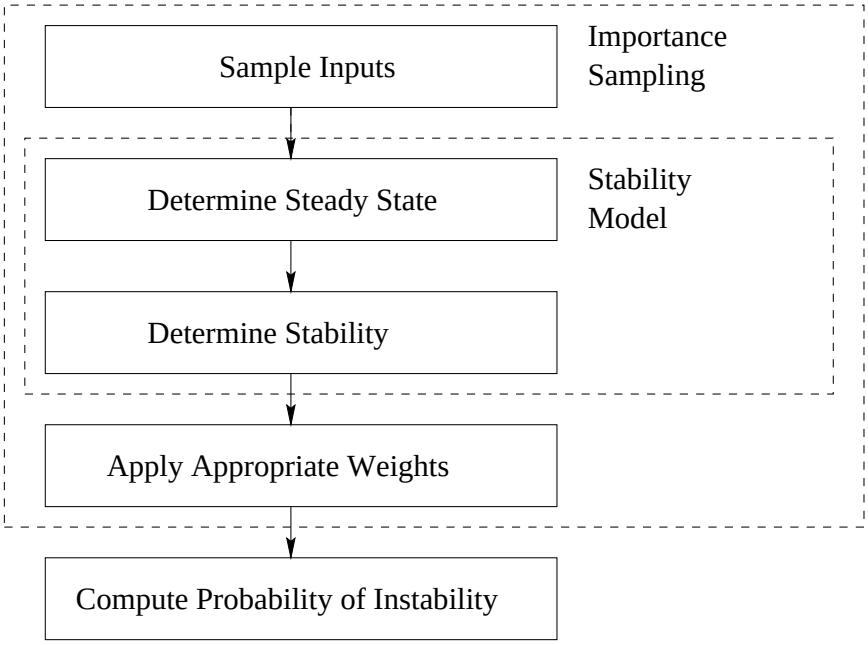

Figure 2-9: Importance Sampling is wrapped around a two stage stability model for probability of instability estimation.

the dynamic model are sampled from scaled or translated probability density functions by the IS procedure. The computation in the stability model is done in two stages – first the steady-state solution is found and then eigenvalue analysis is performed to determine the stability of the steady-state solution to small perturbations. The binary output (stable/unstable) is then re-weighted according to the specifications of

IS and averaging over sufficiently large number of samples is performed.

2.3.1 Inputs and Outputs

For simplicity only the following five parameters, which are thought to be the most important ones, are sampled probabilistically:

- **Inlet distortion amplitude** – The inlet distortion is described in Section 4.1. It requires several parameters all of which, with the exception of the amplitude, are assumed constant. The amplitude is sampled from an exponential distribution that satisfies the following two conditions:

  1. Negative amplitudes have zero probability.
  2. The larger the amplitude, the smaller the probability that it will occur.

  IS via scaling is used for the inlet distortion amplitude.

- **Asymmetric tip clearance nonuniformity** – Unless otherwise stated all simulations are performed with the first harmonic of the asymmetry because, as Graf showed, the influence of the higher harmonics is minimal [1]. The first harmonic corresponds to eccentricity between the rotor and the casing and can be described by an amplitude. This amplitude is sampled from a normal distribution with zero mean, as there is no reason to believe bias exists towards eccentricity. The use of positive and negative amplitudes creates a discontinuity in the phase angle, which will be observed as doubling of the number of peaks of the probability of instability at the end of Chapter 4. IS via scaling is used for the asymmetric tip clearance amplitude.

- **Compressor maximum pressure rise** – Changes in this parameter are due to a number of factors (for example, increased average clearance) that are assumed to be lumped together. The maximum pressure rise is sampled from a normal distribution with mean equal to the nominal maximum compressor pressure rise. IS via translation is used for this model input parameter.

- **Throttle setting coefficient** – This coefficient determines the flow resistance. The pressure drop versus mass flow relationship is:

$$\psi = E\phi^2 \tag{2.14}$$

  The throttle coefficient E is equal to half of the more commonly encountered coefficient K_T [3, 6]. Here E is preferred for sampling convenience. It is sampled from a normal distribution with mean equal to its nominal value. IS via scaling is used for this coefficient.

- **Phase angle between the tip clearance asymmetry and the inlet distortion** – The definition of the phase angle is described in details in section 4.1. The phase angle is assumed to not have a preferred value, thus it is sampled from a uniform distribution covering the interval $[0, 2\pi]$ using simple Monte Carlo.

Table 2.2 shows typical values of the means and standard deviations of the five parameters. Note that the inlet distortion amplitude is controlled by a single parameter because for an exponential distribution the mean and the standard deviation are the same. In the absence of field data, the values of the standard deviations of the maximum compressor pressure rise and the throttle setting are chosen to be one percent of the respective mean values. The value of the standard deviation of the tip clearance corresponds to a percent change in the tip clearance and is considered representative. The actual values used for each simulation are given in Appendix C, but they are similar to the values in Table 2.2.

Table 2.2: Default values of the probabilistic distribution parameters

Parameter	Probabilistic Distribution	Default Mean μ	Default Standard Deviation σ
Inlet Distortion Amplitude	exponential	0.01	0.01
Asymmetric Tip Clearance Nonuniformity Amplitude	normal	0	0.04
Maximum Compressor Pressure Rise	normal	0.8	0.008
Throttle Setting Coefficient	normal	2.9	0.029
Phase Angle	uniform in $[0,\ 2\pi]$	π	Not Applicable

2.3.2 Applications

The proposed probabilistic stability model can be used to perform trade-off studies during the design phase of a jet engine project. Some examples studies are described in this section.

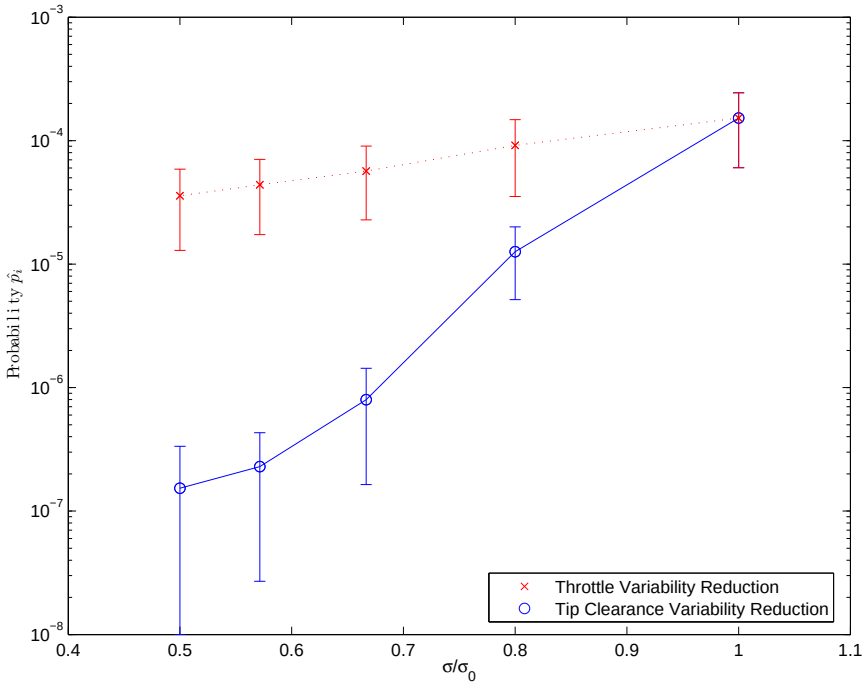

Figure 2-10: Probability of instability (with 99% confidence error bars) as a function of variability which is defined by the standard deviation σ

Suppose designers have two different variability reduction technologies available and they are trying to decide which one to implement. An example in which one technology reduces the throttle setting variability and the other one reduces the variability of the asymmetric tip clearance nonuniformity is shown in Figure 2-10. In addition to the estimated probability of instability for the baseline case ($\sigma/\sigma_0 = 1$) the figure displays the probability of instability as σ is reduced for each of the two inputs. A clear conclusion which technology is more efficient in reducing the number of instabilities can be made from the figure. Even when the 99% confidence intervals are considered, the reduction of the tip clearance asymmetry is the better choice.

A more difficult decision situation is shown in Figure 2-11. It can arise when the stability problems are more severe and a change in mean throttle setting (with a

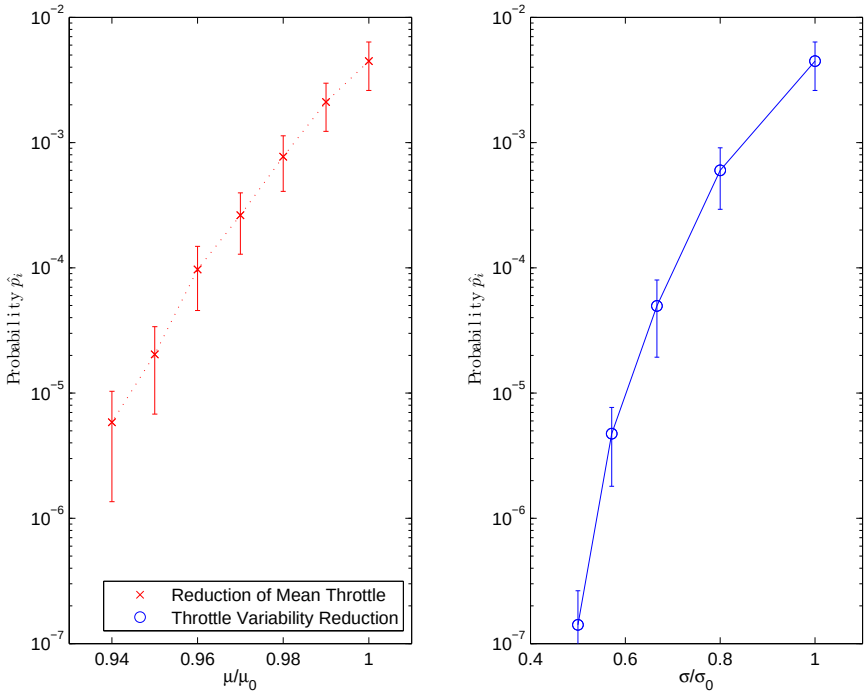

Figure 2-11: A comparison of the effect of mean throttle value reduction to the effect of throttle variability reduction

possible accompanying performance reduction) is considered as a way to bring down the probability of instability. The figure shows a comparison between the changes in the mean throttle setting and reduction of the variability of the throttle setting. If, for example, more than two percent reduction in the nominal throttle setting is unacceptable due to performance constraints, but the probability of instability is still too high, the only way in which the goal can be achieved is by reducing the throttle variability (assuming that the only two levers for influencing the probability of instability are those shown in the figure).

Another possible scenario will be realized if a given level for the probability of instability must be met, for example 1×10^{-5}. Then for the specific distributions of this example the choice is between 40 percent reduction in variability and 6 percent reduction in the nominal (mean) setting. The design process can continue with selection between these two alternatives. The selection is made based on the cost associated with each option.

It is possible for situations to arise in which reduction of the variability is not

achievable and changes of the mean (nominal) values are the only option. For example, suppose there are two options – either to increase the compressor maximum pressure rise by 1% or to decrease the throttle setting E by 2% (presumably reducing the throttle setting E is easier than increasing the pressure rise in a fixed number of stages). Figure 2-12 shows that decreasing the mean throttle setting leads to a lower

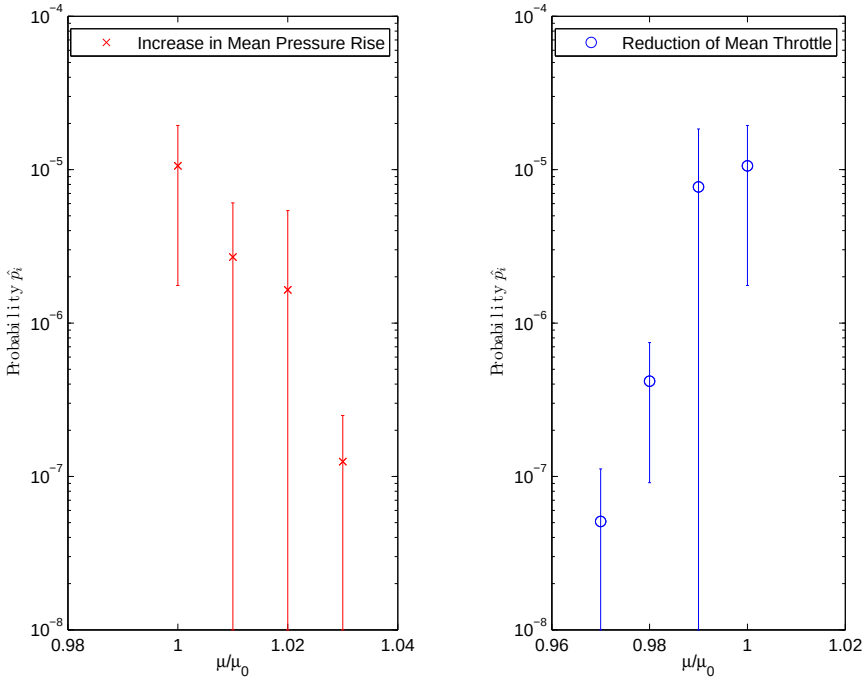

Figure 2-12: A comparison between the effects of increase in mean pressure rise and reduction in mean throttle setting

estimate $\hat{p}_i$.

In summary Figures 2-10, 2-11 and 2-12 show three basic types trade-off studies concerning the probability of instability p_i:

i) effects of variability of one parameter versus the effects of variability in another parameter

ii) effects of the variability of one parameter versus the effects of changing the mean of another (or the same) parameter

iii) effects of the mean value of one parameter versus the effects of the mean value of another parameter.

2.4 The Effects of Aging

The analysis in the previous section assumes that the probability of instability does not change in time. As jet engines age, however, the probability of instability increases as clearances open up, blades and seals wear, etc. The Importance Sampling methodology can be modified to compute different quantities of interest defined over a given time interval of interest. The quantity of interest is identified as the probability of instability before reaching a given number of flight cycles. Other quantities of interest such as the expected number of instabilities in a fleet with a given distribution of ages can also be simulated, but will not be considered here.

It is assumed that all engines in the fleet have the same age. This assumption is not a fundamental limitation because by the use of Bayes' law the probability of instability for a given age distribution can be determined and the calculation proceed in a similar manner.

The simulation technique defined in this section will be referred as time-variant (TV) simulation and the simulation technique from the previous section will be referred as time-invariant (TI) simulation from now on.

2.4.1 Description

The data flow in the model when deterioration is included is different than the data flow presented earlier. The new information flow sequence is shown in Figure 2-13. The input parameters of the model are separated into two categories: engine specific and operating environment specific. The engine specific parameters are sampled once and then the engine is subjected to a sequence of stability simulations. In each simulation, the operating environment conditions are sampled independently with the engine parameters modified on each cycle to include the deterioration. If a linear deterioration model is assumed then in each simulation the compressor maximum pressure rise is decreased by a fixed amount and a new set of environment parameters (for example, inlet distortion amplitude) is generated. This is repeated for a given number of cycles, for example 2000, which might represent the time until the first

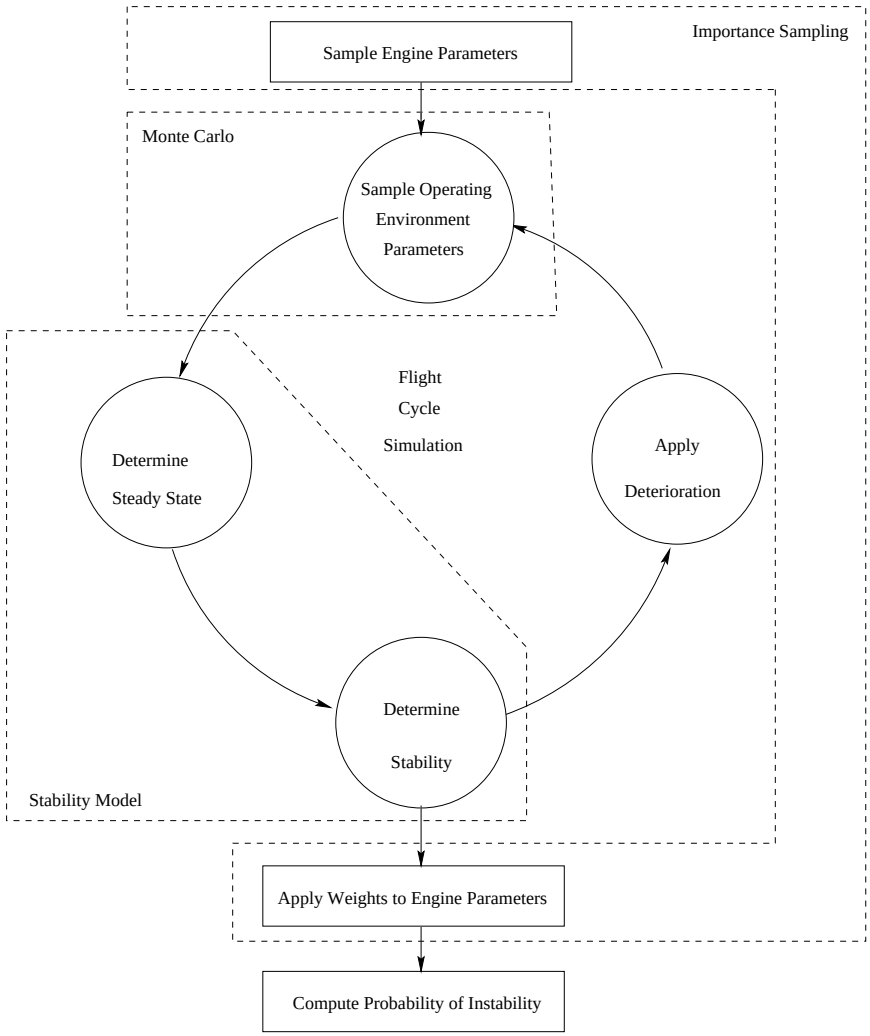

Figure 2-13: Logical data flow in the deterioration simulations – after the manufacturing parameters of an engine are sampled, it is subjected to a sequence of stability simulations for which the operating environment conditions are re-sampled with each simulation cycle and the engine parameters are updated for deterioration effects.

Table 2.3: Deterioration rates

Parameter	Deterioration Rate Γ [1/cycle]
Maximum Compressor Pressure Rise	$+1.82 \times 10^{-5}$
Tip Clearance Asymmetry Amplitude	$+3.58 \times 10^{-6}$
Throttle Setting	-8.06×10^{-6}

scheduled overhaul. Once the 2000 simulations cycles are completed, a new engine is sampled and it is again subjected to the cycling simulation for the same number of cycles.

A linear deterioration model is used for all simulations. For example, the maximum compressor pressure rise equation is:

$$\psi_{max} = (\psi_{max})_0 - \Gamma(k-1), \tag{2.15}$$

where ψ_{max} is the maximum compressor pressure rise on cycle k, $(\psi_{max})_0$ is the initial maximum compressor pressure rise and Γ is the maximum pressure rise loss per cycle. The value of Γ has been determined from the data of Richardson and James [20, 21] by converting the efficiency losses to effective pressure ratio reductions. The pressure ratios are converted to pressure rises using the inverse of the equations in Appendix A and the resulting difference between the pressure rises is then divided by the number of cycles for which the data was obtained. A similar approach is used for the asymmetric tip clearance and the throttle setting coefficient. The actual values used in all simulations are shown in Table 2.3 (as obtained from the data of Richardson and James [20, 21]). The value of Γ for the throttle setting coefficient E is negative because the throttle setting needs to get closer to the stability limit with time in order to provide the same power output.

In the TV simulations the operating environment parameters should not be Importance Sampled any more. The reason originates in the inherited behavior of multi-dimensional IS. For simplicity consider 500 flight cycles and let the random variables Y_1, Y_2, Y_3, ..., Y_{500} with PDFs $f(Y_1)$, $f(Y_2)$, ..., $f(Y_{500})$ represent the amplitude of the inlet distortion on each cycle. Let $X = X(Y_1, Y_2, ..., Y_{500})$ be the random variable indicating whether the system is stable or unstable (0 or 1). From the definition of

$\hat{p_i}$ the following equation is obtained

$$\hat{p_i} = E[X] = \int X f(Y_1) f(Y_2) ... f(Y_{500}) dY_1 dY_2 ... dY_{500}, \tag{2.16}$$

and when it is rewritten in a form appropriate for IS Equation 2.16 becomes

$$\hat{p_i} = \int X \frac{f(Y_1)}{f^*(Y_1)} \frac{f(Y_2)}{f^*(Y_2)} ... \frac{f(Y_{500})}{f^*(Y_{500})}) f^*(Y_1) f^*(Y_2) ... f^*(Y_{500}) dY_1 dY_2 ... dY_{500}. \tag{2.17}$$

The problem comes from the $\frac{f(Y_k)}{f^*(Y_k)}$ terms. If the engine shows an instability on the first cycle then the $\frac{f(Y_k)}{f^*(Y_k)}$ terms for $k \geq 2$ do not matter because in this case X depends only on Y_1 and $\frac{f(Y_1)}{f^*(Y_1)}$ is presumably small if $f^*(Y_1)$ has been chosen appropriately. If there is no instability on the first cycle, but on the second one then X depends only on Y_1 and Y_2, but now $\frac{f(Y_1)}{f^*(Y_1)}$ does not need to be small even though $\frac{f(Y_2)}{f^*(Y_2)}$ is small. Actually given that there is no instability on the first cycle, it is known that Y_1 is in the region where $\frac{f(Y_1)}{f^*(Y_1)}$ is large, making the IS procedure relative to Y_1 inefficient compared to Monte Carlo. This deteriorates the quality of the estimate relative to Y_1, but as more and more of Y_k are considered the estimate deteriorates relative to all previous inputs Y_1, Y_2, ..., Y_{k-1}. In the TI simulations this effect did not show up to a significant degree because if the fraction $\frac{f(Y)}{f^*(Y)}$ was large, but the choice of function $f^*(Y)$ was appropriate then $X(Y) = 0$ eliminating the large term from the integral. Here, in the TV simulations, this is not the case: $X = 1$ because the engine showed instability exactly on the k-th cycle. The performance deterioration is significant and becomes worse if more than 500 flight cycles are considered. For this reason the environment parameters are subjected to Monte Carlo, rather than IS. IS is retained in the simulation of the engine parameters.

2.4.2 Applications

The information obtained from simulations including engine deterioration can be used in the same manner as the time-invariant trade-off studies. Table 2.4 contains simulation data for a baseline case and four hypothetical alternatives. In all cases

Table 2.4: Comparison between the effects of aging and the effects of variability and mean values

Case	Lower Bound	Probability $\hat{p}_i$	Upper Bound
Baseline	-7.04×10^{-5}	6.64×10^{-4}	1.39×10^{-3}
Reduced Throttle Deterioration	-9.51×10^{-6}	3.20×10^{-4}	6.50×10^{-4}
Reduced Tip Clearance Deterioration	-1.24×10^{-5}	1.91×10^{-4}	3.96×10^{-4}
Reduced Throttle Variation	$+6.87 \times 10^{-5}$	4.23×10^{-4}	7.78×10^{-4}
Reduced Nominal Throttle	-1.81×10^{-4}	2.42×10^{-4}	6.66×10^{-4}

500 flight cycles are simulated. Suppose that a choice between two different materials to be used for a given component (for example turbine seals) has to be made. One of the materials might be easier to process and therefore leads to less component variation, but wears at a higher rate than the other one. It is not an obvious choice to which material is the better one. The variability and the wear rate can be used to generate a table similar to 2.4. The easier to process material corresponds to the fourth row and the other one corresponds to the second row. The table shows that the less prone to wear material is the better design choice because it leads to lower probability of instability. Even though this conclusion cannot withstand arguments that the 99% confidence intervals overlap significantly for it to be unconditionally true, the intervals can be tightened by using more samples and/or problem specific Importance Sampling distributions.

Simulations including the effects of aging can also be used in setting the overhaul period. Figure 2-14 shows the probability of instability as a function of the number of flight cycles before overhaul. If the tolerable level of probability of instability is known, then the corresponding overhaul cycle length can be read off from the figure.

This figure also underlines the advantages of Importance Sampling. The circle and triangle show the probability of instability for 500 flight cycles and the upper 99% confidence limit as predicted by the Monte Carlo method. The lower bound is not shown because it is negative. In this case Monte Carlo obtained about the same confidence intervals as Importance Sampling with 4 times more samples. If IS is run for the same number of samples as the Monte Carlo method, the much

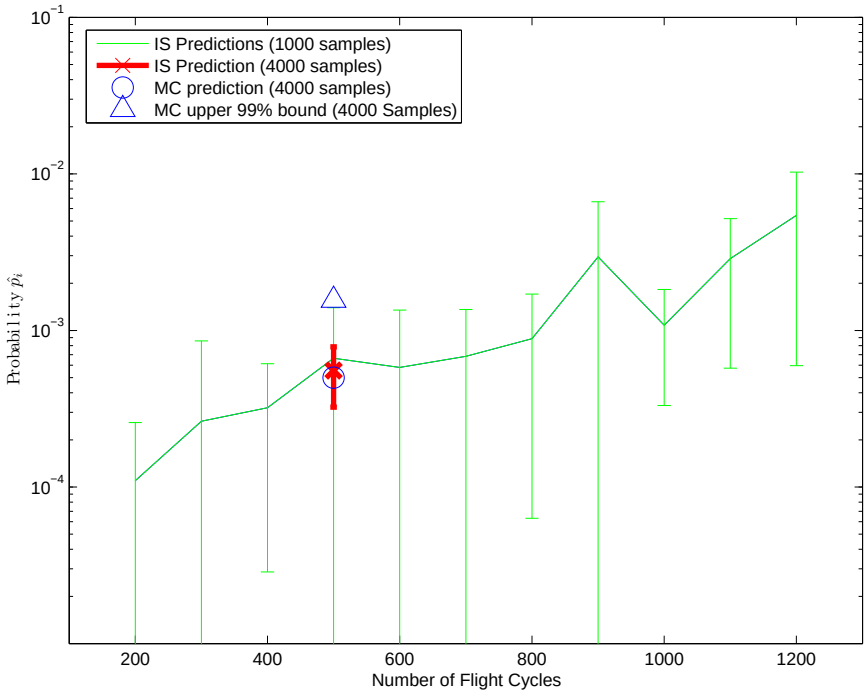

Figure 2-14: Probability of instability as a function of the number of flown flight cycles before engine overhaul (or decommission)

better confidence interval and prediction as represented by the thick red line are obtained. Better optimization of the IS parameters and use of more advanced IS techniques tailored specifically at the problem at hand could lead to one or two orders of magnitude reduction in the required number of samples. The exact value of the probability p_i also influences the performance ratio between the Monte Carlo method and Importance Sampling – the lower the probability p_i, the larger the benefits of Importance Sampling.

Chapter 3

A Probabilistic View of Stability Margins

Stability Margin (SM) is a widely used measure of the stability of jet engines and compression systems. One possible definition of SM is [22]

$$SM = \frac{\pi_{inst} - \pi_{act}}{\pi_{act}}, \tag{3.1}$$

where π_{inst} is the pressure ratio at the instability and π_{act} is the actual operating pressure ratio. The two pressure ratios are taken at the same corrected mass flow $\dot{m}_{corr}$. The pressure ratio π is defined as:

$$\pi = \frac{p_{t3}}{p_{t2}}, \tag{3.2}$$

where p_{t2} is the total pressure at the compressor inlet and p_{t3} is the total pressure at the compressor exit. The SM is a measure how far the actual operating point is from the instability line. The SM is shown in Figure 3-1. The detailed equations by which the figure is constructed from the $\phi - \psi$ compressor and throttle curves are outlined in Appendix A.

In Figure 3-1 the operating line corresponds to constant throttle setting coefficient E, while the nominal stability line corresponds to the points to which the peak of

the compressor pressure rise curve maps at different corrected speeds. The nominal stability line is for condition of no distortion, no tip clearance asymmetry, no peak variation line and has throttle setting $E = 3.2$. Point B lies on the real stability line and it is the place where the stability point at fixed corrected flow moves to when distortion, tip clearance asymmetry and peak variation are added. SM represents the vertical distance from the actual operating point A to the point of instability onset B. The distance from A to C is the available stability margin (aSM) and the distance between B and C is the required stability margin (rSM). The required stability margin is the minimum margin necessary to guarantee stable operation. The stability margin can be expressed as the difference between aSM and rSM:

$$SM = aSM - rSM \tag{3.3}$$

In order for Equation 3.3 to hold, the definition of rSM is

$$rSM = \frac{\pi_C - \pi_B}{\pi_A}, \tag{3.4}$$

while the definition of aSM follows Equation 3.1:

$$aSM = \frac{\pi_C - \pi_A}{\pi_A}. \tag{3.5}$$

The pressure ratios at A, B and C are denoted with π_A, π_B and π_C, respectively. Due to the "nondimensionalization" of the pressure ratio with the actual pressure ratio π_{act} the stability margin can be directly read off the figure.

The details of the process of obtaining the probability of instability from SM are given in Section 3.3. The general procedure consists of three steps:

i) estimate rSM for each factor influencing the stability

ii) add all rSMs

iii) assume normal distribution for the sum and estimate the probability of instability from it.

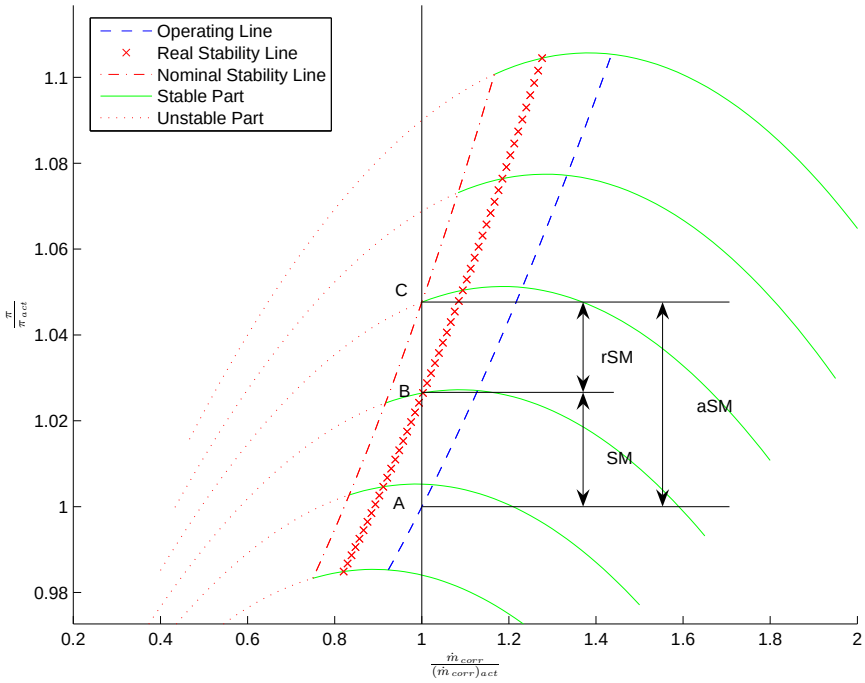

Figure 3-1: Graphical representation of the required stability margin (rSM), the available stability margin (aSM) and the stability margin (SM)

The following two sections exemplify some of the errors made in these steps.

3.1 The Additivity of Margins

The required stability margin (rSM) as shown in Figure 3-1 depends on the position of point B, which itself depends on the factors reducing the stability of the jet engine. When only the effect of the maximum pressure rise is considered, point B will be at a given location and rSM will have some value rSM_{MPR}. When only the effect of the inlet distortion is considered, point B will be at another location and rSM will have some value rSM_{ID}. When both, the effect of the maximum pressure rise and the effect of the inlet distortion, are considered together, point B will be at a third location and rSM will have some other value rSM_{MPR+ID}. There is no fundamental reason why the dynamic model should give values such that $rSM_{MPR+ID} = rSM_{MPR} + rSM_{ID}$.

The lack of additivity of SM is shown in Figure 3-2 which displays contours of the

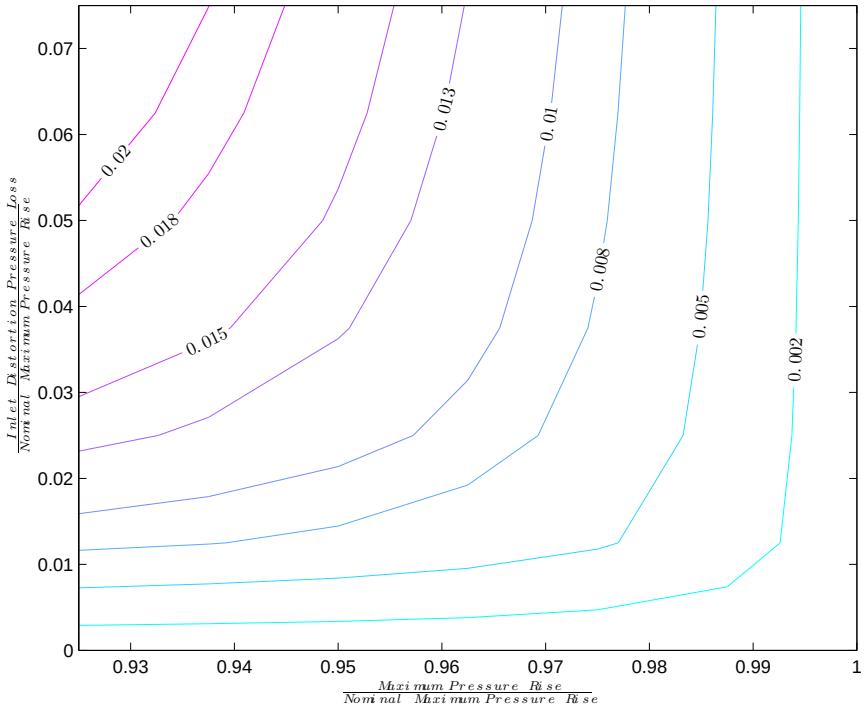

Figure 3-2: Contours of constant relative error RE in a case without asymmetric tip clearance variation

relative error RE,

$$RE = \frac{rSM_{MPR} + rSM_{ID} - rSM_{MPR+ID}}{rSM_{MPR+ID}}. \tag{3.6}$$

The figure shows that the larger the departures from the nominal values of the two factors, the larger the relative error RE. With only two factors the maximum error obtained is about 2% of the rSM, but when a third factor is added the relative error grows up to about 10% which makes it non-negligible. This is illustrated by Figure 3-3 which shows similar contours of constant error at one percent asymmetric tip clearance amplitude.

3.2 Nonlinearity of Margins

The non-additivity of rSM does not manifest itself only when several different factors, whose effects need to be added, are considered, but also when a *single* factor is

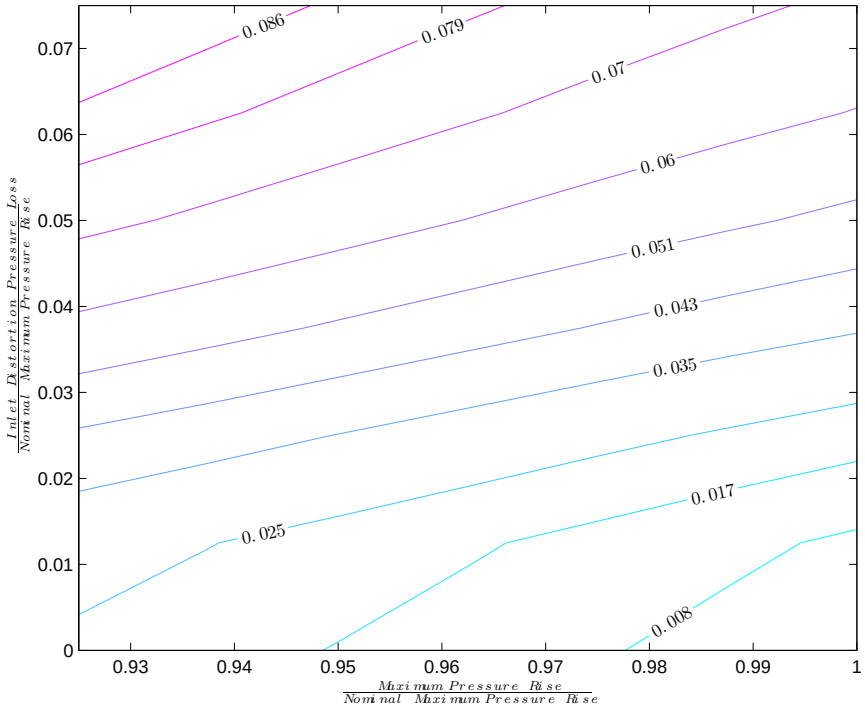

Figure 3-3: Contours of constant relative error in a case with one percent asymmetric tip clearance amplitude

considered. If rSM was additive (i.e. $rSM(a+b) = rSM(a)+rSM(b)$) then doubling the cause when a *single* instability cause was considered should double the rSM. Equivalently rSM should be linear relative to the cause. This is not always the case as it can be seen from Figure 3-4. The stability degrading factor considered is the nonuniform tip clearance and its amplitude is shown on the horizontal axis. The required stability margin is computed for two different pressure rise curves. It can be seen that for the steep pressure rise curve the dependence is approximately linear except very close to zero. This happens because the section of the pressure rise curve which has very high curvature is small and even small tip clearance deviation pushes the operating point beyond it. The situation is different for shallower pressure rise curves. The curvature is smaller, but it remains significant for a large portion of the curve causing the initial deviation from linearity in the tip clearance - rSM relationship observed for the second pressure rise curve in the figure. Beyond 3% tip clearance amplitude the linearity assumption holds with reasonable accuracy. A description of the curve numbering nomenclature used in this figure and in next section can be

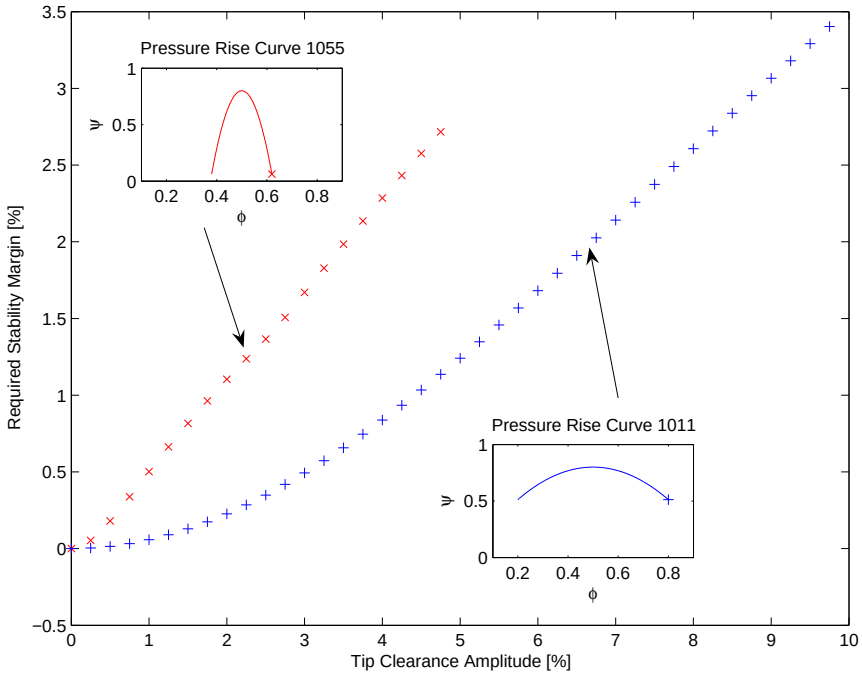

Figure 3-4: Required stability margin as a function of the asymmetric tip clearance amplitude for two different compressor pressure rise curves

found in Appendix B.

Other factors in addition to tip clearance asymmetry could result in nonlinear behavior. Figure 3-5 shows rSM for different levels of the maximum compressor pressure rise and for different amplitudes of the inlet distortion. Weak nonlinearities are visible in both plots, even though the ranges shown are very large and will not be encountered in practice. When smaller, more realistic, ranges are considered the linear approximation holds with acceptable accuracy for these two cases.

3.3 Probability of Instability Predictions Based on Margins

The prediction of the probability of instability based on stability margin assumes that the overall stability margin distribution is normal. Figure 3-6 illustrates the process of determining the probability of instability from the stability margin. The area under the tail of the distribution and to the left of the zero represents the probability of

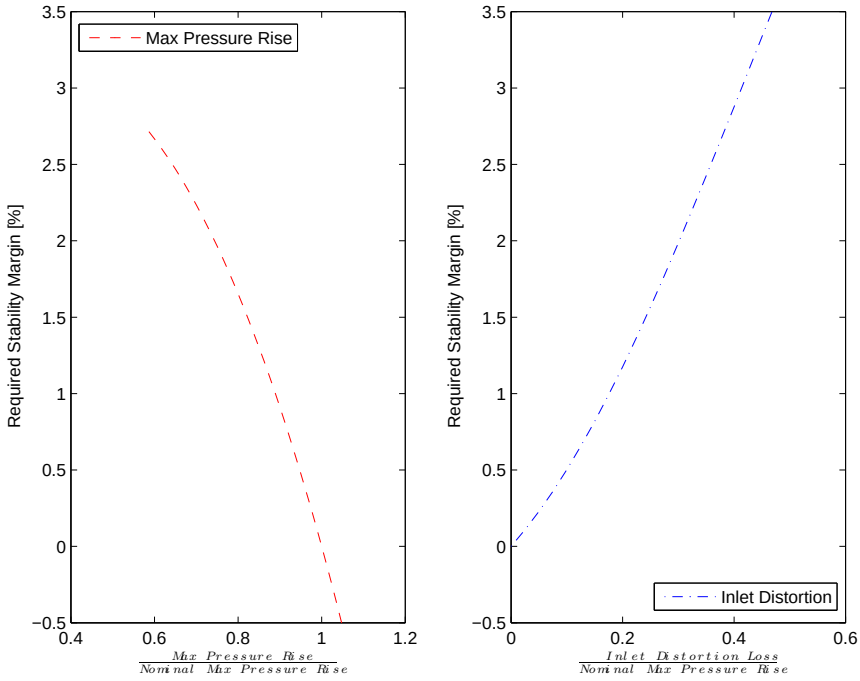

Figure 3-5: Weak nonlinearities in the required stability margin for variations in the maximum pressure rise and the inlet distortion loss also exist.

instability.

Computationally the mean and the standard deviation of SM can be determined from Monte Carlo simulations that, in addition, produce the distributions of SM. For example, if three factors are considered and rSM is assumed additive then:

$$rSM_{total} = rSM_1 + rSM_2 + rSM_3, \tag{3.7}$$

where rSM_{total} is the total required stability margin and rSM_1, rSM_2, rSM_3 are the required stability margins for each of the factors. Given Equation 3.7 the following way of computing the total mean and standard deviation can be devised:

$$\mu_{rSM_{total}} = E[rSM_{total}] = E[rSM_1] + E[rSM_2] + E[rSM_3] = \tag{3.8}$$

$$= \mu_{rSM_1} + \mu_{rSM_2} + \mu_{rSM_3} \tag{3.9}$$

$$\sigma_{rSM_{total}} = \sqrt{var(rSM_{total})} = \tag{3.10}$$

$$= \sqrt{var(rSM_1) + var(rSM_2) + var(rSM_3)} = \tag{3.11}$$

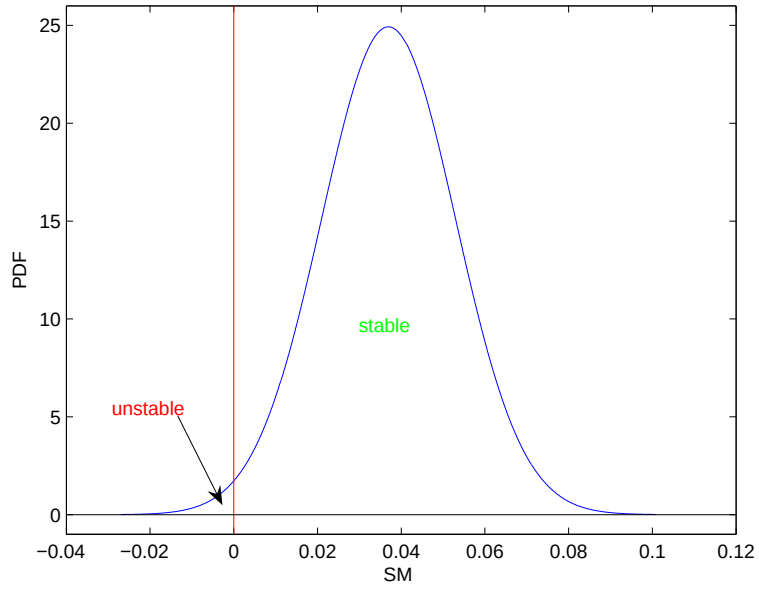

Figure 3-6: The Use of Normal Distribution for Prediction of Probability of Instability

$$= \sqrt{\sigma_{rSM_1}^2 + \sigma_{rSM_2}^2 + \sigma_{rSM_3}^2}, \tag{3.12}$$

where μ and σ stand for the mean and the standard deviation respectively. It will be shown that there are important cases when the normal distribution assumption used to evaluate the probability of instability does not hold and leads to significant errors. A better estimate of the probability of instability can be obtained by counting the number of times SM is less than zero and dividing the result by the total number of Monte Carlo samples.

3.3.1 The Importance of the Dominating Effects

A prediction based on the normality assumption can be quite good if the inputs under consideration are normal and the dependence of SM on them is approximately linear. One such case is shown in Figure 3-7. The only input considered in this case is variation of the maximum pressure rise, which has a normal distribution. The distribution of SM comes out approximately normal as confirmed by the normal probability plot, indicating that good agreement between the direct counting of the

number of negative SM and the prediction based on the normal curve fit can be expected. The two predictions as cited in the figure come out to within a percent of each other.

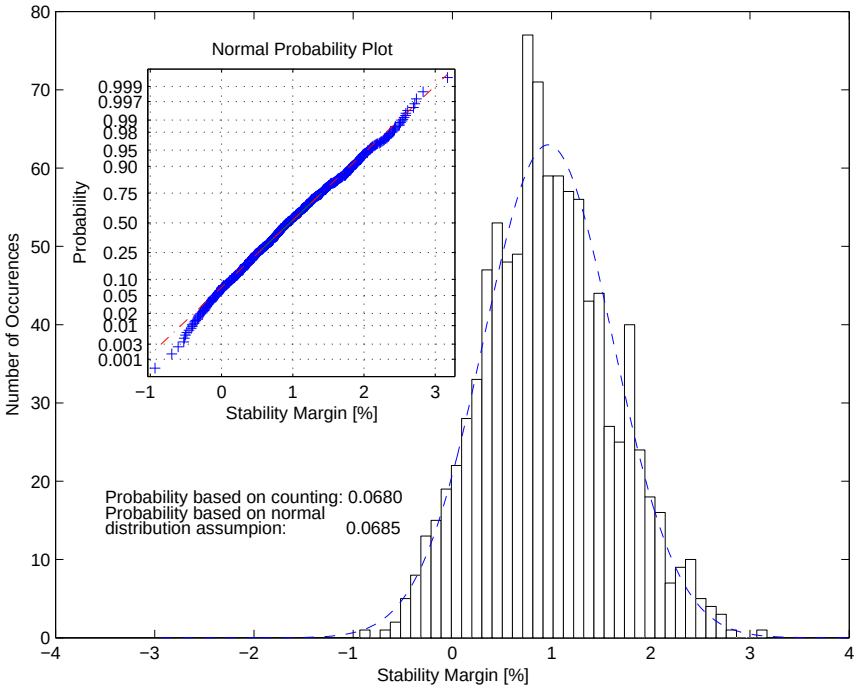

Figure 3-7: Histogram of stability margin when the maximum pressure rise has variability of 6%; the distribution of stability margin is very close to normal and the agreement between the probabilities obtained by the two methods is very good.

For inputs that are not normally distributed, the assumption of output normality can be poor, for example, the inlet distortion is exponentially distributed and therefore its PDF is very far from normal. The distribution of SM when the only factor considered is inlet distortion is shown in Figure 3-8. The distribution is clearly not normal as indicated by the normal probability plot. Agreement between the two probability prediction methods cannot be expected and indeed the disagreement is roughly 20%.

The SM distributions presented above were obtained by considering a single input to the model, but similar behavior can be observed when several inputs are considered. Figure 3-9 shows a case when asymmetric tip clearance, inlet distortion and the maximum pressure rise are all probabilistically sampled. The mean levels of the three

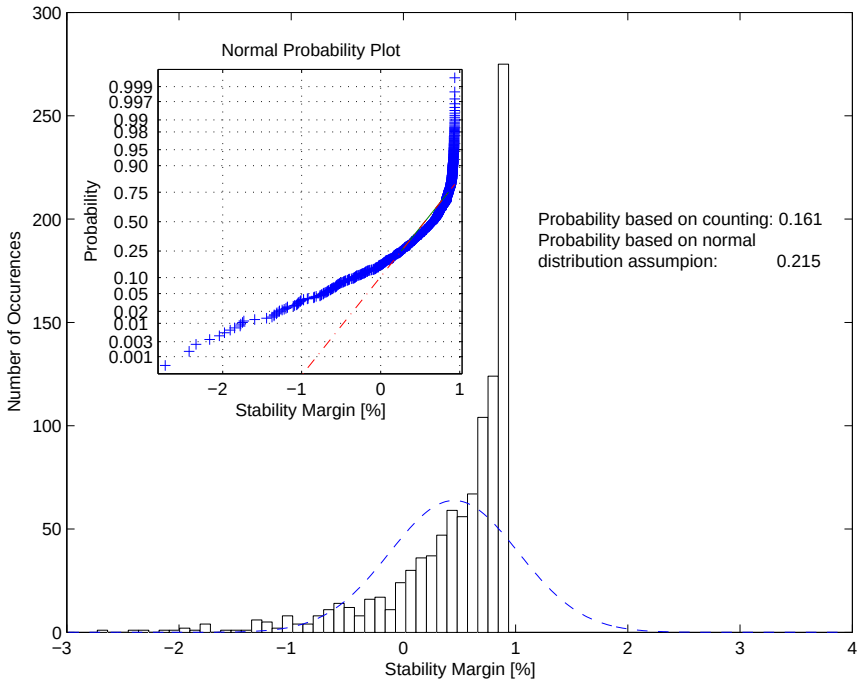

Figure 3-8: Histogram of stability margin when the mean inlet distortion pressure loss is 5% of the maximum pressure rise; the distribution of stability margin is clearly not normal and this is reflected in the disagreement between the probabilities obtained by the two methods.

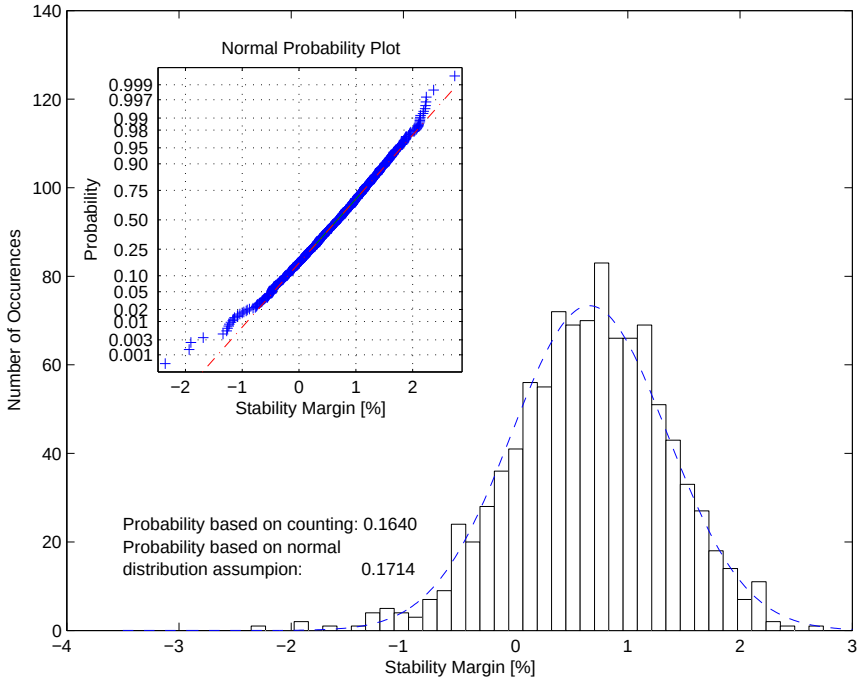

Figure 3-9: Stability margin distribution in the absence of dominating non-normal effects

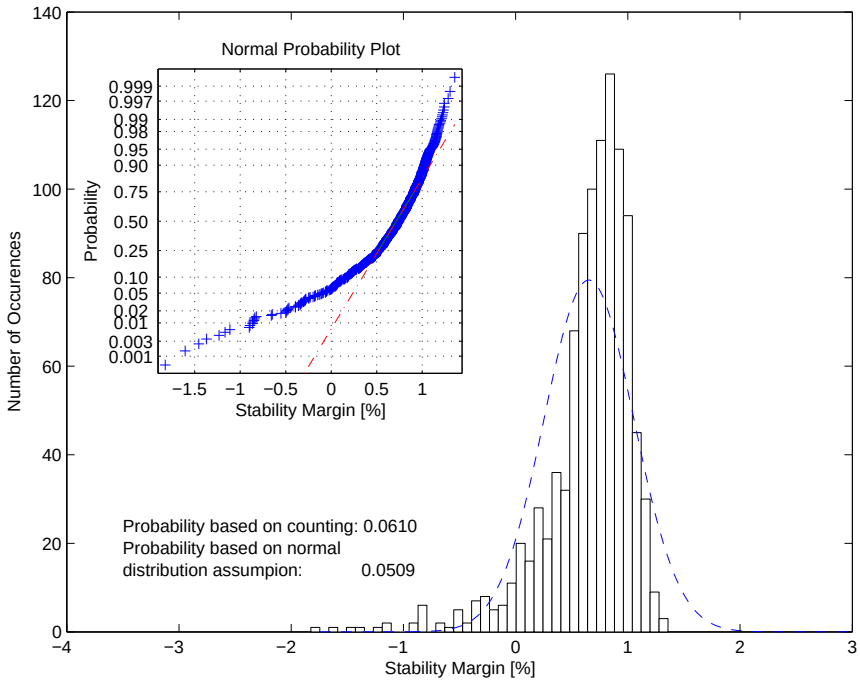

Figure 3-10: Stability margin distribution in the presence of dominating non-normal effects

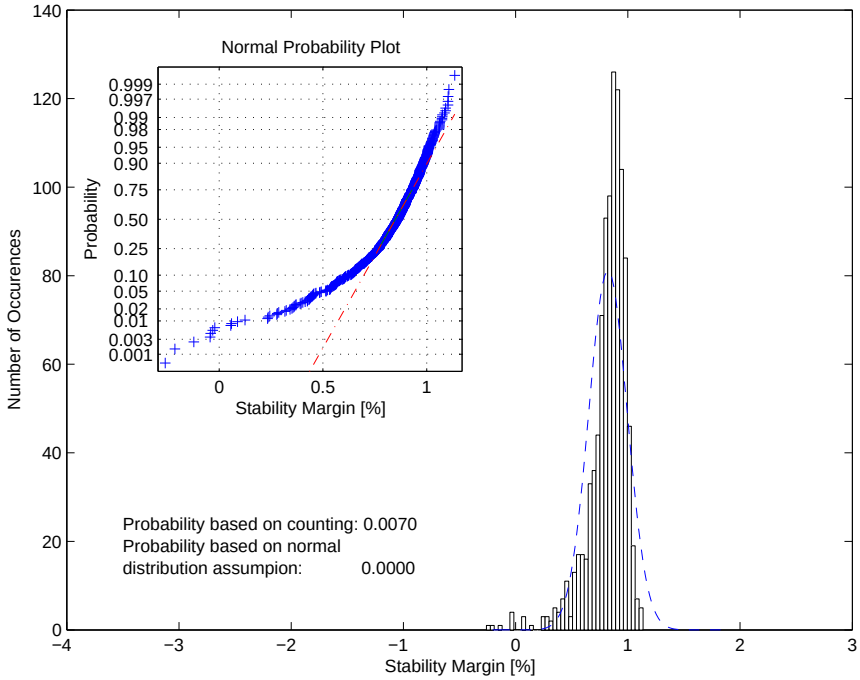

Figure 3-11: Stability margin distribution in the presence of dominating non-normal effects; note that in this case the probability based on counting also begins to lose attractiveness because there are too few samples with negative margins (7 out of 1000 samples)

inputs have been chosen so that there is no dominating non-normal effect. In such case the agreement between the two predictions is relatively good. Cases when the mean levels of the inputs are such that a dominating factor is present are shown in Figures 3-10 and 3-11. The normal fit is not appropriate and a large difference in the predictions produced by the normal fit and the direct counting is observed. In the last case the prediction based on counting the number of negative SMs cannot be trusted because there are too few samples with negative SM. Therefore the direct counting method even though "exact" in its nature can generate poor quality predictions if the probability of instability is small and no or few actual cases of negative SM are recorded.

An estimate in the counting method can be obtained by increasing the number of samples (and therefore the execution time). Importance Sampling cannot be applied to generate histograms of SM in this case because IS modifies the distributions. The mean and the standard deviations of SM can still be estimated with IS if necessary.

3.3.2 Comparison Between the Approaches for Predicting the Probability of Instability

Table 3.1 contains the numerical values of the probability of instability for the cases considered in the previous section. In addition, it contains the predictions obtained via IS to allow for comparison between the two approaches. The first column with numbers contains the probability of instability obtained on the basis of the normality assumption. The second column with numbers shows the probability as computed by counting the number of negative SMs. This column is also labeled "MC over margin" because the counting of the margins is equivalent to Monte Carlo method applied over the margins. The last column with numbers contains the probability as predicted by Importance Sampling or Monte Carlo (in parenthesis). Monte Carlo as a specific case of Importance Sampling is used in the first few cases because the probability to be simulated is not small enough to justify the use of IS.

The table once again illustrates that the prediction using the normality assumption

Table 3.1: Probability of instability as predicted by the different methods. The format of the numbers is $\hat{p}_i \pm z$ where z is the 99% confidence interval

Case	SM normality assumption	SM counting/ MC over margin	IS (or MC)	Figure
F_1	0.0685	0.0680 ± 0.0239	(0.0560 ± 0.0218)	3-7
F_2	0.2150	0.1610 ± 0.0349	(0.1840 ± 0.0368)	3-8
F_3	0.1714	0.1640 ± 0.0351	(0.1730 ± 0.0359)	3-9
F_4	0.0509	0.0610 ± 0.0227	(0.0680 ± 0.0239)	3-10
F_5	0.0000	0.0070 ± 0.0079	0.0028 ± 0.0013 (0.0050 ± 0.0067)	3-11
F_6	5.2042×10^{-15}	0 ± 0	$1.5629 \times 10^{-4} \pm 7.6681 \times 10^{-5}$	
F_7	4.3984×10^{-31}	0 ± 0	$9.4933 \times 10^{-6} \pm 7.9947 \times 10^{-6}$	

does not behave properly when the SM distribution is not normal. The predictions based on the normality assumption in the last two cases are clearly unrealistically low. The SM counting method also begins to give significant errors when the probability drops to 5×10^{-6}. For such cases, the SM counting does not encounter any events during the simulation and predicts zero probability.

In summary, the Importance Sampling technique from the previous chapter (supplemented with Monte Carlo when the probabilities to be estimated are large) is the most general and gives the most realistic estimates of the three methods compared here because it does not rely on any assumptions about normality, linearity and additivity.

Chapter 4

Inlet Distortion – Asymmetric Tip Clearance Interaction

4.1 Model Description

Inlet distortion and asymmetric tip clearance are both circumferential disturbances to uniform annular flow. Their interaction can lead to enhancement or suppression of the growth of the circumferential instability waves. It is to be expected that when the distortion is aligned with a portion of increased tip clearance the compression system will be less stable than if the distortion is aligned with a region of reduced tip clearance.

There are models that consider inlet distortion and asymmetric tip clearance separately [6, 1]. They solve in one or another form the following equation for the axial flow coefficient ϕ:

$$\frac{p_4 - p_{t2}}{\rho U^2} = \psi(\phi) - \lambda \frac{\partial \phi}{\partial \theta} - \frac{r\mu}{U} \frac{\partial \phi}{\partial t}, \tag{4.1}$$

where U is the wheel speed, ρ is the density, λ and μ are parameters describing the fluid inertia (defined in Appendix D), p_4 is the plenum pressure and p_{t2} is the inlet stagnation pressure. To unify the two models we note that the inlet distortion enters via inlet stagnation pressure p_{t_4} while the asymmetric tip clearance enters the equation via the pressure rise $\psi(\phi)$ so the two effects are decoupled from each

other and can be imposed separately. The computational procedure developed by Hynes and Greitzer is extended to account for variable pressure rise $\psi = \psi(\phi, \theta)$. The circumferential angle θ is added as a parameter of ψ because every point on the circumference has a different local pressure rise curve [1]. Following Graf, the pressure rise curve at each point on the circumference is computed from the local tip clearance using the correlation of Smith [18] that for each additional percent tip clearance there is a corresponding 5% reduction in the maximum pressure rise.

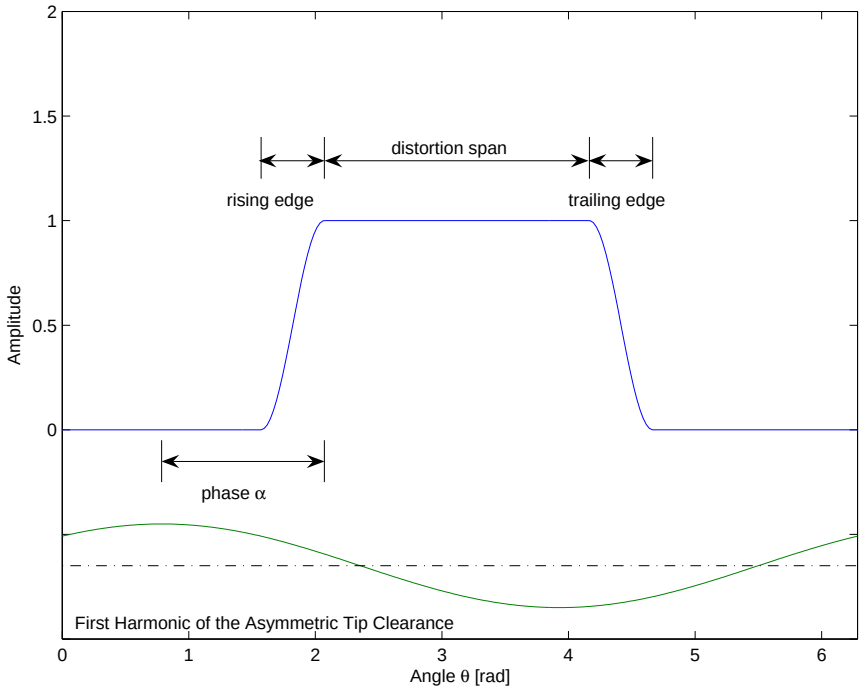

Figure 4-1: Inlet distortion shape and positioning relative to the asymmetric tip clearance

The phase angle between the inlet distortion and the tip clearance asymmetry determines whether the two add constructively or destructively. The definitions of the phase angle α, the span, and the trailing and raising edges of the inlet distortion are shown in Figure 4-1. The tip clearance asymmetry is assumed to be sinusoidal in shape. This is not a significant restriction as it has been shown that the first harmonic of the tip clearance asymmetry is the most important one [1]. The inlet distortion is assumed to be almost square in shape, having a flat top where the loss is constant and two half-sine shaped edges. These edges are added in order to improve

the resemblance to a real non-screen induced inlet distortion, which does not have discontinuous jumps. In the results to follow, the length of the edges is $\pi/10$ and the length of the flat section is $2\pi/3$. Even though the first few harmonics of the distortion are the most important ones the length of the edges can significantly modify their amplitudes and therefore the edges were deemed a necessary addition. The phase angle α is defined as the angle between the point of largest tip clearance and the end of the rising edge (the beginning of the flat section) of the distortion.

4.2 Parametric Study

4.2.1 The Effect of Operating Point

Figure 4-2 shows plots of the largest real part of the eigenvalues as a function of

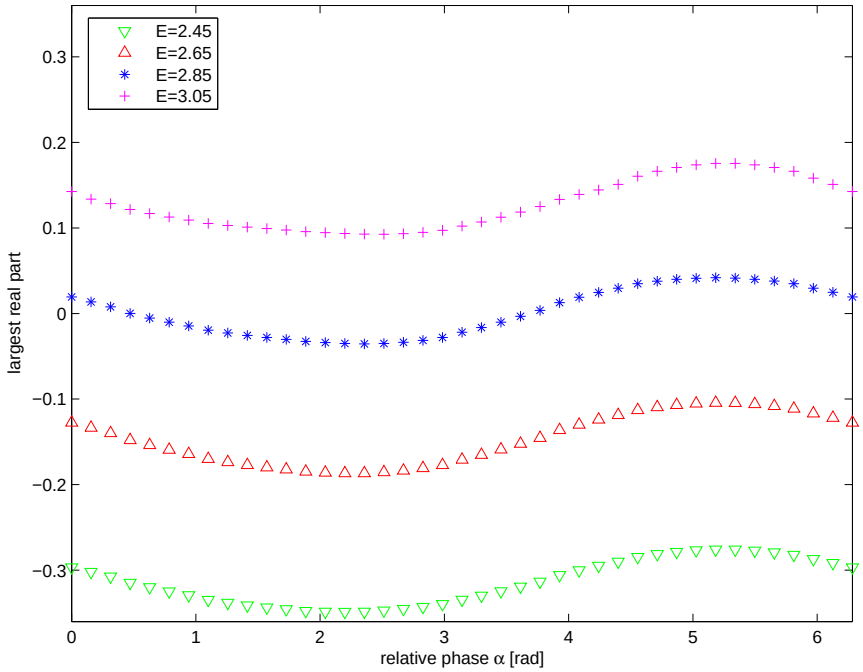

Figure 4-2: Dependence of the Phase Effect on the Operating Point (Throttle Setting E)

the phase angle α at different levels of the throttle setting E. In one of the cases, the curve crosses the zero line implying that the phase itself can drive the stability, with some phase angles leading to stable conditions and some phase angles leading

to unstable conditions. The approximately sine-wave shape of the curves shown can be explained with the sine shape of the tip clearance asymmetry. It is to be expect that the constructive and destructive effects of the distortion at α and $\alpha + \pi$ are the approximately same, but have different directions.

4.2.2 The Effect of Curve Shape

The effect of different curve shapes was explored by Graf [1], who found that some pressure rise curves tend to cause slower decay rates (larger negative real parts of the system eigenvalues) for the circumferential waves than others. A similar effect is observed when the interaction of the asymmetric tip clearance with the distortion is considered. Figures 4-3 and 4-4 display the dependence of the largest real part of

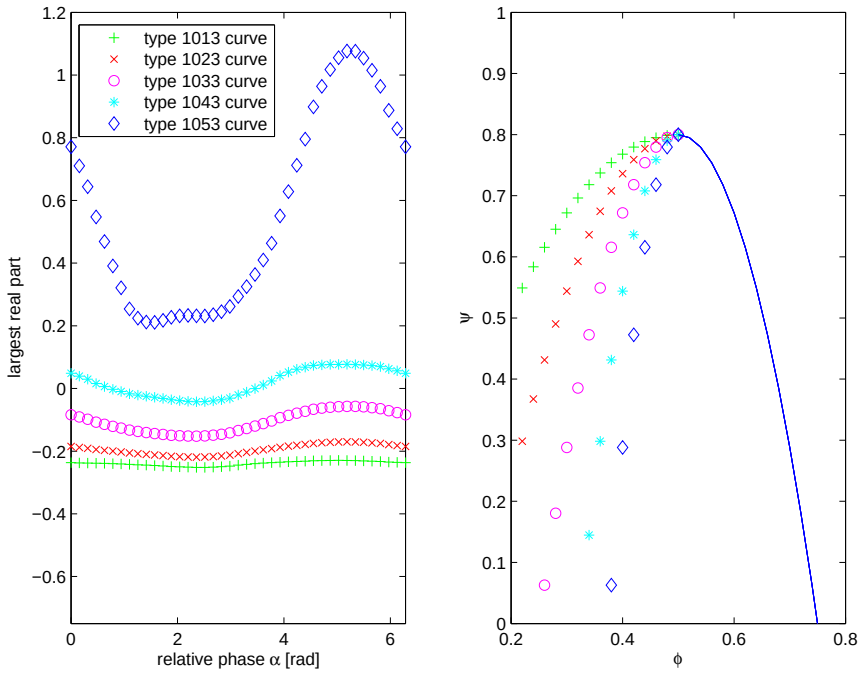

Figure 4-3: Dependence of the Phase Effect on the Curve Shape to the Left of the Peak

the eigenvalues on the phase for different pressure rise curves. All pressure rise curves considered have the same maximum pressure rise and are subjected to inlet distortion and tip clearance asymmetry with the same amplitudes. The throttle setting is also kept the same in all simulations. Figure 4-3 considers pressure rise curves which are

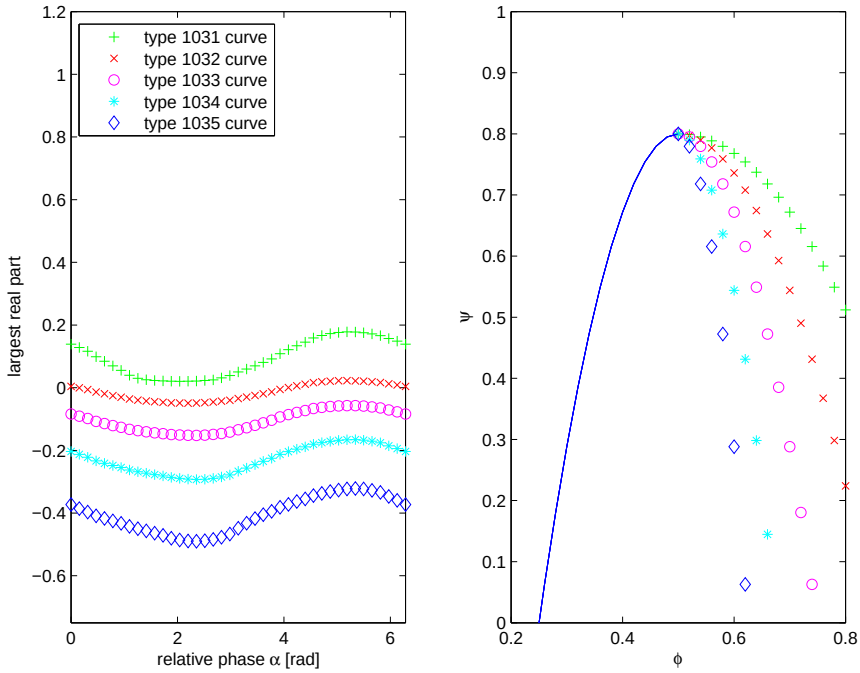

Figure 4-4: Dependence of the Phase Effect on the Curve Shape to the Right of the Peak

the same to the right of the peak, but become steeper and steeper to the left of the peak (see Appendix B for the curve type nomenclature). From the investigation of Graf it is known that the steeper the curve on the left the more unstable the points of the circumference operating in that region and therefore the less stable the whole system is. The same effect is observed here. Figure 4-4 shows the analogous behavior for curve variations on the right of the peak. In this case, the steeper the curve on the right is, the more stable the compression system is.

4.2.3 Other Effects

The dependence of stability on two other parameters is shown in Figure 4-5. It has been found by Graf that the higher harmonics of the tip clearance asymmetry have much less influence on the stability than the first harmonic [1]. The first plot shows that this continues to be the case when inlet distortion is added. In the particular case shown, the first harmonic leads to instabilities at all phase angles while the second and the third harmonic lead to very stable configurations. The amplitudes of the

asymmetric tip clearance in all three cases is the same.

The second plot in the figure shows the dependence of the largest real part of the eigenvalues on the phase α for different values of the distortion span angle. As it is to be expected, the larger the distortion span, the larger the portion of the curve above zero, i.e., the more likely the instability is.

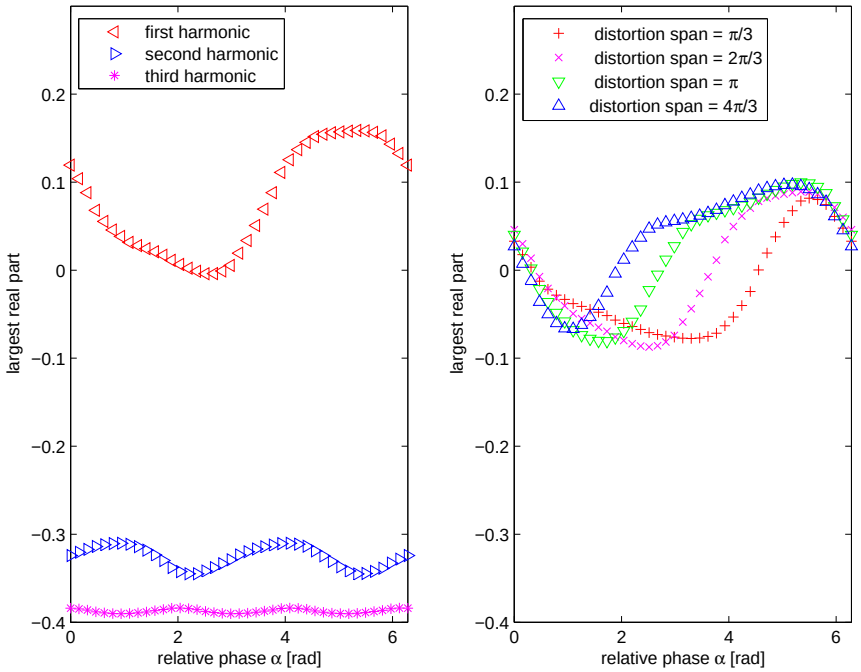

Figure 4-5: Dependence of the Phase Effect on the Harmonic Number and the Distortion Span Angle

4.3 The Probabilistic Effect of the Phase

Given that the phase angle has such a large effect on the stability of the system, it is interesting to check what its effect on the probability of instability is.

In the stability margin approach one of the most obvious disadvantages of SM is that it cannot capture the effect of the phase angle. Figure 4-6 displays contours of constant relative error in the stability margin, when simple additivity is assumed and no provisions for the phase angle are made. In two of the cases the error is on the order of 2-3 percent and probably can be neglected without any serious consequences.

In the other two cases shown, the error in the margin is the order of 20 to 50 percent and cannot be ignored. Furthermore, the errors in these two cases are in different directions because one of those cases corresponds to perfect in-phase alignment of the distortion and the tip clearance asymmetry and the other one corresponds to perfect out of phase alignment. Given the large error in the stability margin, large errors in the prediction of the probability of instability are possible.

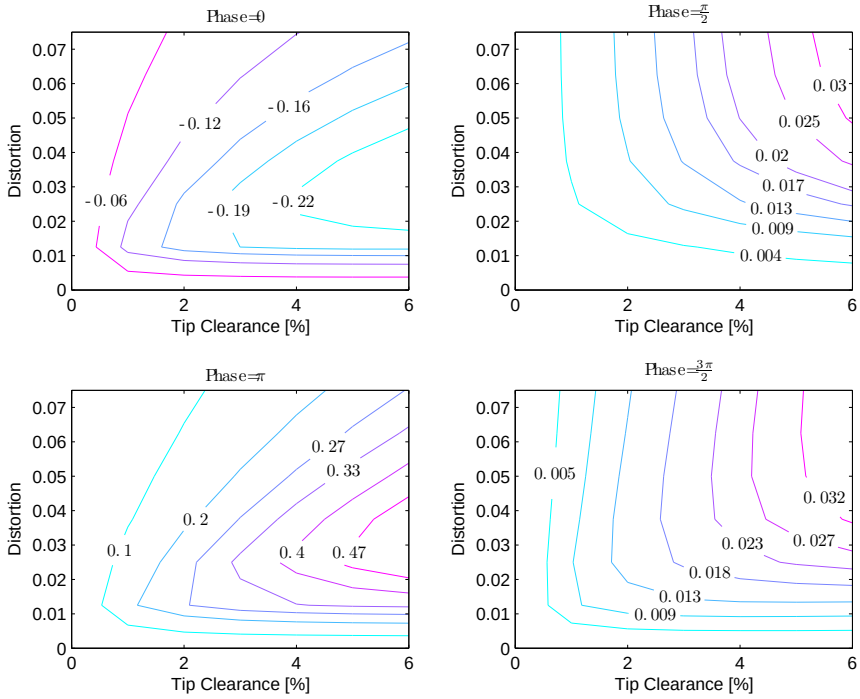

Figure 4-6: Contours of relative error made when the additivity assumption for stability margin is used.

The errors in the stability margin approach can be contrasted to straightforward inclusion of the phase angle as an input in the Importance Sampling approach. The probabilistic distributions of the other parameters are the same as the ones used in Chapter 2 and the importance sampling parameters, a and c, are also kept the same. The probability of instability $\hat{p_i}$ together with its confidence intervals is shown as a function of the phase angle in Figure 4-7. Peaks in the probability can be seen when the distortion and the tip clearance asymmetry are aligned and valleys when they are not. The two peaks are a result of the probabilistic distribution used for the tip clearance amplitude. Specifically ,the tip clearance amplitude is sampled from

a normal distribution with zero mean. Therefore, negative values are as likely as positive values. The effect of a negative value for the amplitude is to invert the phase, more specifically to add π radians to it and thus causing the second peak in the figure.

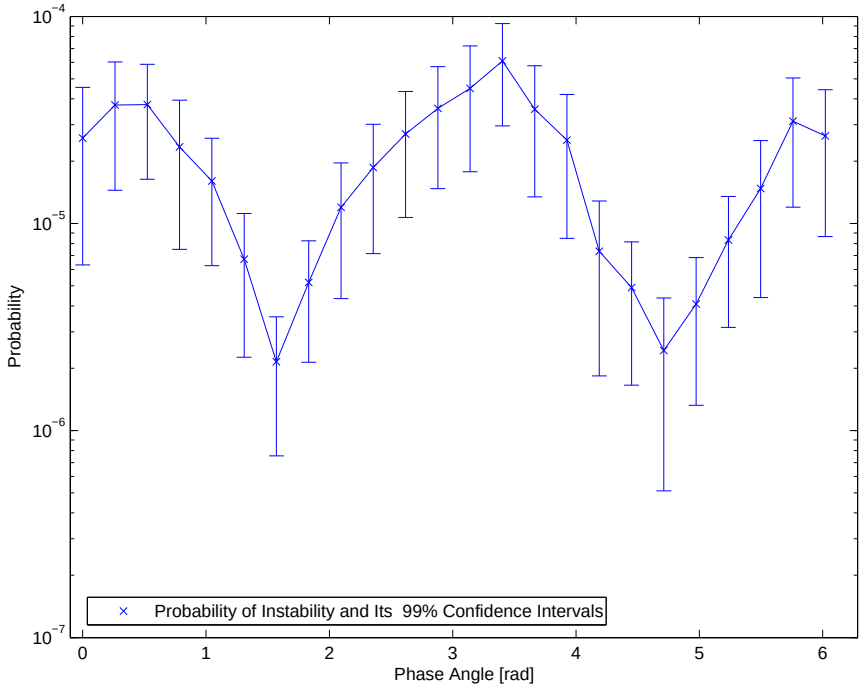

Figure 4-7: Probability of instability as predicted by importance sampling for different phase angles between the inlet distortion and the tip clearance asymmetry

Table 4.1: Probability of instability predictions

Angle	IS estimate of p_i	SM estimate of p_i
0	2.587×10^{-05}	1.865×10^{-16}
$\frac{\pi}{2}$	2.149×10^{-06}	8.034×10^{-16}
π	4.493×10^{-05}	9.434×10^{-17}
$\frac{3\pi}{2}$	2.437×10^{-06}	1.489×10^{-18}
Random	2.400×10^{-05}	9.333×10^{-14}
Inlet Distortion only	5.482×10^{-07}	2.947×10^{-85}
Tip Clearance Asymmetry only	3.734×10^{-07}	2.080×10^{-20}

A comparison between the values for the probability of instability predicted using Importance Sampling and Stability Margin is shown in table 4.1. In all cases, the predictions obtained via stability margin calculation are unrealistically low. The inlet

distortion only case and the tip clearance only case are provided for reference and once again underline the problem which the stability margin approach has with non-normal distributions. The probabilistic distribution of the phase angle α in the case labeled "Random" is uniform as there is no reason for a preferred angle to exist. The stability margin approach fails to capture the qualitative behavior of the probability of instability as a function of the phase angle. The large quantitative difference in the numbers for the two columns of the table are due to additivity and normality assumptions in the SM approach.

Chapter 5

Conclusion

5.1 Summary

The following is a summary of the major findings and accomplishments of this work:

- A probabilistic treatment of compression system instability based on Importance Sampling and dynamical models [6, 1] has been developed. It has been shown that the approach is capable of estimating the probability of instability even when it is very small and when a Monte Carlo simulation with comparable confidence intervals would require excessive computational times. The advantage of Importance Sampling over ordinary Monte Carlo is realized by scaling and translating the input distributions. A few possible applications of the probabilistic approach in the early design stages of new jet engine development projects have been outlined. The approach has been adapted to incorporate aging effects.

- Shortcomings of the traditional stability margin approach have been identified. Specifically, it was shown via examples that the common assumptions that stability margin is additive, linear and normally distributed do not always hold. The largest errors come from the normality assumption and can be avoided by the use of Monte Carlo over the margin instead of the normal fit. The Monte Carlo over the margin, however, has its own problem of requiring large number

of samples for small confidence intervals.

- Importance Sampling estimates were compared to estimates obtained via the two approaches based on stability margin. It was found that the approach assuming normality of the distribution gives inferior results compared to the other estimation techniques. The Monte Carlo over the margin approach has performance comparable to the Importance Sampling, but inserts an unnecessary step for margin computation.

- The effect of the interaction between asymmetric tip clearance and inlet distortion was modeled. It was found that the interaction is strongly dependent on the relative phase angle between the two. It was shown that situations when the relative phase by itself drives the instability can occur. Overall the model agreed qualitatively with the expected trends known from experience or other models. It was shown that the more traditional stability margin approach does not capture neither the qualitative, nor the quantitative behavior of the probability of instability in the presence of the effects of the relative phase.

In conclusion, a new approach based on a known dynamical model and a probabilistic technique specifically tailored to the problem at hand – Importance Sampling – has been suggested. Its advantages over regular Monte Carlo methods and stability margin approaches have been illustrated by a set of examples and possible issues within the stability margin approach have been identified.

5.2 Future Work

A few possible directions of improvement in the order of importance are:

- Comparison of the predicted probabilities of instabilities against real instability data from the field. This should be done for both, the time-variant and the time-invariant simulation modes.

- The dynamical model used in this work is incompressible in its nature. For a more realistic simulation a compressible model is needed.
- A more realistic deterioration model can be incorporated into the simulation. The current model assumes linear deterioration, but a model with high wear-and-tear profile in the first few flight cycles will be more realistic.
- Once real inputs for an engine from the field are available the importance sampling methods and distributions can be finely tuned for improved performance on the problem at hand.
- The factors leading to the probabilistic nature of the maximum compressor pressure rise need to be differentiated and fully investigated.

Appendix A

Pressure Rise Curve to Compressor Map Conversion

A typical compressor pressure rise characteristic used in the simulations is presented in Figure A-1. The dividing point between the stable and unstable region is assumed to be the peak of the characteristic [4]. A compressor map showing the corrected mass-flow versus the pressure ratio is obtained from the pressure rise characteristic using the following equations:

$$\pi = 1 + (\frac{\rho n^2 U_{nom}^2}{p_t})\psi \tag{A.1}$$

$$\dot{m}_{corr} = m\frac{\sqrt{T_t}}{p_t} = (AU_{nom}n\sqrt{\frac{\rho}{p_t R}})\phi, \tag{A.2}$$

where U_{nom} is the nominal wheel speed, p_t is the inlet stagnation pressure, ρ is the density, n is the wheel speed fraction, T_t is the inlet stagnation pressure, ψ is the pressure rise and ϕ is the mass flow coefficient.

A sample compressor map assuming $A = 1$ m^2, $U_{nom} = 100$ m/s, $p_t = 1.013 \times 10^5$ Pa and $\rho = 1.225$ kg/m^3 is shown in Figure A-2. The percentages next to each line indicate the fractional speed n. Figure A-2 can be transformed into Figure 3-1 by normalization of the vertical and horizontal scales with the actual pressure ratio π_{act} and the actual corrected mass-flow $(\dot{m}_{corr})_{act}$.

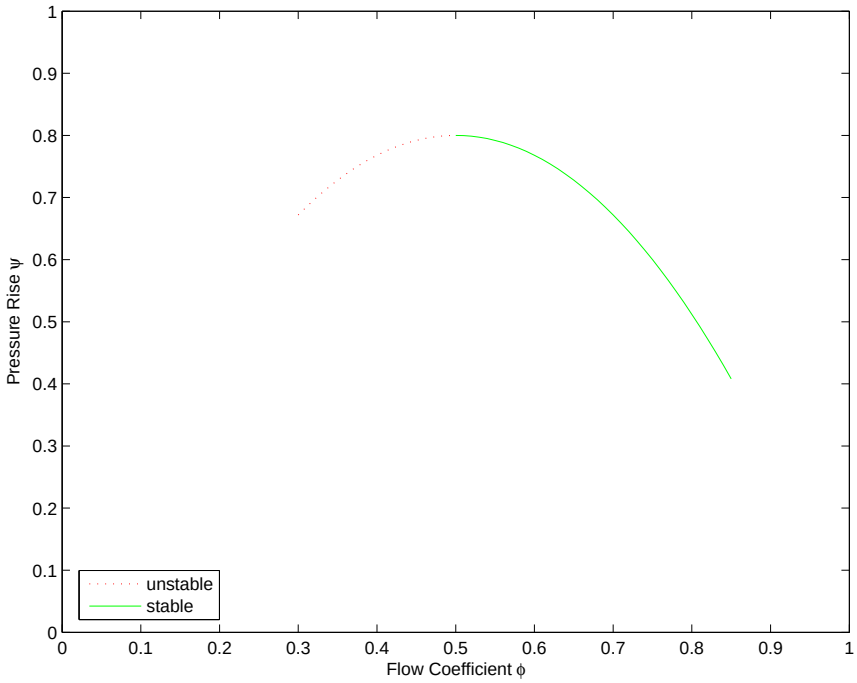

Figure A-1: Sample compressor pressure rise characteristic with the stable and unstable regions identified

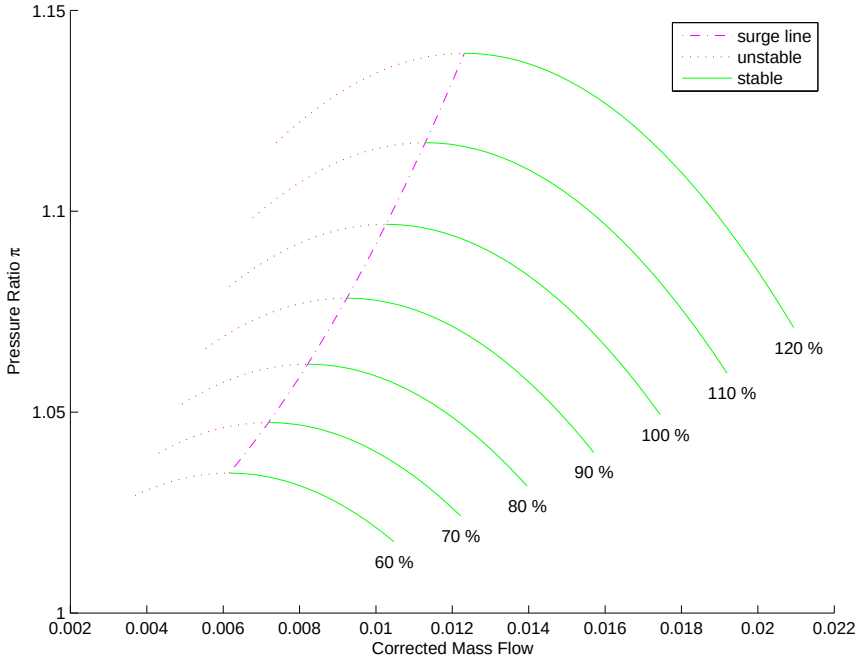

Figure A-2: Compressor map generated from the sample pressure rise characteristic shown in Figure A-1

Appendix B

Compressor Pressure Rise Curves

The compressor pressure rise curves used in this thesis have been generating by "gluing" together pieces of parabolas. The different pieces are shown in Figure B-1 and the gluing has been performed at the top of each parabola where the slope of the curve is zero. The type number associated with each curves is a four digit number. The first two digits are 1 and 0 and provide distinction from all previous curve type definitions used within the project code (unique identification numbers are easier to use than context dependent identification numbers). The third digit is associated with the curve on the left of the peak. The larger the digit is, the steeper the curve is. The exact equation of the parabola is given by:

$$\psi = 0.8 - 1.8 * 2^k * (\phi - 0.5)^2 \text{ for } 0 \leq \phi \leq 0.5, \tag{B.1}$$

where k is the third digit in the curve type number. The same equation is used for the right hand side of the curve:

$$\psi = 0.8 - 1.8 * 2^l * (\phi - 0.5)^2 \text{ for } 0.5 \leq \phi \leq 1, \tag{B.2}$$

where l is the fourth digit in the curve type number.

A few examples of different curve types are shown in Figure B-2.

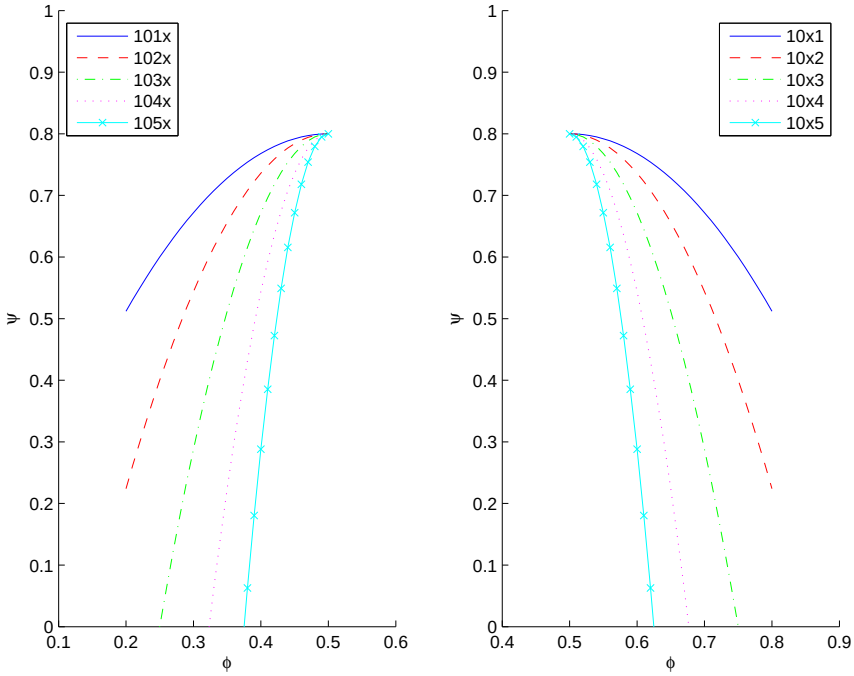

Figure B-1: Left of the peak and right of the peak curve shapes and their naming conventions

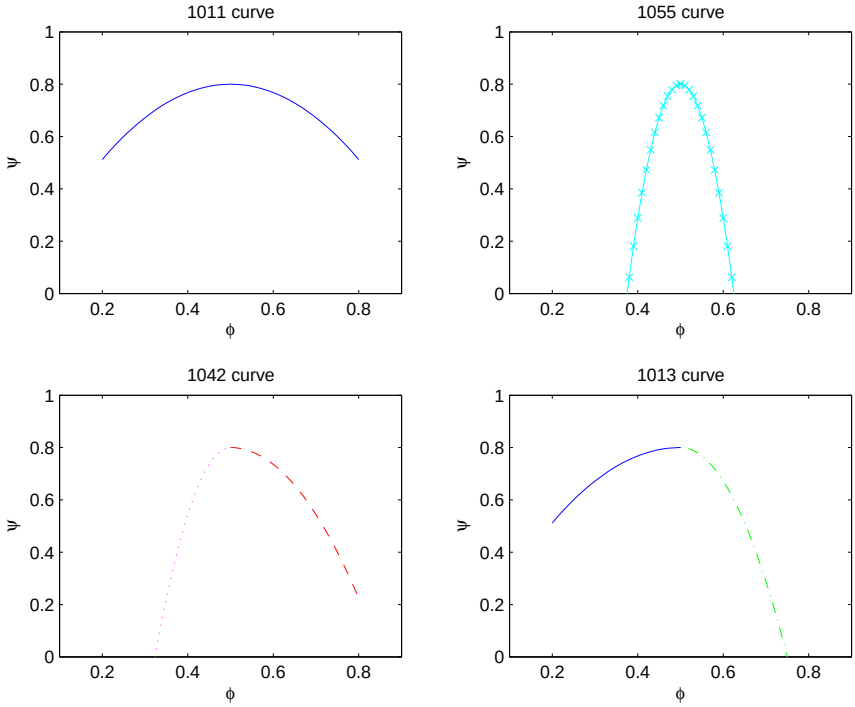

Figure B-2: Examples of curves assembled from left of the peak and right of the peak pieces

Appendix C

Tables of Simulation Parameters

This appendix contains the minimum set of input values required for reproduction of the results shown within this thesis. If within a section of the following four tables there is an unspecified input then it either has the default value if it is a required input for that particular simulation, or its value is irrelevant because it is not an input parameter for that particular simulation. For example the section on Table 4-7 does not contain a number for the harmonic number of the tip clearance amplitude because it has the default value of 1; alternatively for the same table, the standard deviation of the maximum pressure rise is not given because the maximum pressure rise is not varied during the simulations incorporated into the table.

Table C.1: Parameters used for generation of the figures and tables in Chapter 2

Global parameters			
Parameter	Value	Parameter	Value
Greitzer's B parameter	0.05	λ parameter of the Hynes-Greitzer model	1.0
Inlet distortion span angle	$\frac{2\pi}{3}$	μ parameter of the Hynes-Greitzer model	1.01
Parameters for Figures 2-10, 2-11 and 2-12			
Parameter	Value	Parameter	Value
Curve type	1011	Mean throttle setting $E_{nom} = (\mu_E)_0$	2.9
St. Dev. of inlet distortion $(\sigma_{ID})_0$	$0.02(\mu_{MPR})_0$	St. Dev. of tip clearance amplitude $(\sigma_{TC})_0$	1%
Mean maximum pressure rise $(\mu_{MPR})_0$	0.8	Sample Size	1000
St. Dev. of maximum pressure rise $(\sigma_{MPR})_0$	$0.015(\mu_{MPR})_0$	St. Dev. of throttle setting $(\sigma_E)_0$	$0.02E_{nom}$
Tip clearance harmonic	1	Phase angle α	$\frac{\pi}{2}$
Parameters for Table 2.4			
Parameter	Value	Parameter	Value
Mean throttle setting $E_{nom} = (\mu_E)_0$	2.9	St. Dev. of throttle setting $(\sigma_E)_0$	$0.01E_{nom}$
Reduced throttle deterioration	0.5Γ	Reduced tip clearance deterioration	0.2Γ
Reduced throttle variation	$0.5(\sigma_E)_0$	Reduced nominal throttle	$0.99E_{nom}$
No maximum pressure rise variation; no inlet distortion variation			
Parameters for Figure 2-14			
Parameter	Value	Parameter	Value
Mean throttle setting $E_{nom} = (\mu_E)_0$	2.9	St. Dev. of throttle setting $(\sigma_E)_0$	$0.01E_{nom}$
St. Dev. of inlet distortion $(\sigma_{ID})_0$	$0.02(\mu_{MPR})_0$	St. Dev. of tip clearance amplitude $(\sigma_{TC})_0$	1%
Mean maximum pressure rise $(\mu_{MPR})_0$	0.8	Curve type	1011
No maximum pressure rise variation			

Table C.2: Parameters used for generation of the figures and tables in Chapter 3

Parameters for Figures 3-2 and 3-3			
Parameter	Value	Parameter	Value
Nominal maximum pressure rise $(\mu_{MPR})_0$	0.8	Tip clearance amplitude	1%
Mean throttle setting $E_{nom} = (\mu_E)_0$	2.9	Curve type	1011
Tip clearance harmonic	1	Phase angle α	$\frac{\pi}{2}$

Parameters for Figure 3-4			
Parameter	Value	Parameter	Value
Nominal maximum pressure rise $(\mu_{MPR})_0$	0.8	Mean throttle setting $E_{nom} = (\mu_E)_0$	2.9
Tip clearance harmonic	1		

Parameters for Figure 3-5			
Parameter	Value	Parameter	Value
Nominal maximum pressure rise $(\mu_{MPR})_0$	0.8	Curve type	1011
Mean throttle setting $E_{nom} = (\mu_E)_0$	2.9		

Parameters for Figure 3-7			
Parameter	Value	Parameter	Value
Nominal maximum pressure rise $(\mu_{MPR})_0$	0.8	Mean throttle setting $E_{nom} = (\mu_E)_0$	2.9
St. Dev. of maximum pressure rise $(\sigma_{MPR})_0$	$0.06(\mu_{MPR})_0$	Sample Size	1000

Table C.3: Parameters used for generation of the figures and tables in Chapter 3 (continued)

Parameters for Figure 3-8			
Parameter	Value	Parameter	Value
Nominal maximum pressure rise $(\mu_{MPR})_0$	0.8	Mean throttle setting $E_{nom} = (\mu_E)_0$	2.9
St. Dev. of inlet distortion amplitude $(\sigma_{ID})_0$	$0.04(\mu_{MPR})_0$	Sample Size	1000

Parameters for Figure 3-9			
Parameter	Value	Parameter	Value
Nominal maximum pressure rise $(\mu_{MPR})_0$	0.8	Mean throttle setting $E_{nom} = (\mu_E)_0$	2.9
St. Dev. of maximum pressure rise $(\sigma_{MPR})_0$	$0.06(\mu_{MPR})_0$	Std. Dev. of tip clearance amplitude	1%
St. Dev. of inlet distortion amplitude $(\sigma_{ID})_0$	$0.025(\mu_{MPR})_0$	Sample Size	1000

Parameters for Figure 3-10			
Parameter	Value	Parameter	Value
Nominal maximum pressure rise $(\mu_{MPR})_0$	0.8	Mean throttle setting $E_{nom} = (\mu_E)_0$	2.9
St. Dev. of maximum pressure rise $(\sigma_{MPR})_0$	$0.015(\mu_{MPR})_0$	Std. Dev. of tip clearance amplitude	1%
St. Dev. of inlet distortion amplitude $(\sigma_{ID})_0$	$0.025(\mu_{MPR})_0$	Sample Size	1000

Parameters for Figure 3-11			
Parameter	Value	Parameter	Value
Nominal maximum pressure rise $(\mu_{MPR})_0$	0.8	Mean throttle setting $E_{nom} = (\mu_E)_0$	2.9
St. Dev. of maximum pressure rise $(\sigma_{MPR})_0$	$0.0075(\mu_{MPR})_0$	Std. Dev. of tip clearance amplitude	1%
St. Dev. of inlet distortion amplitude $(\sigma_{ID})_0$	$0.0125(\mu_{MPR})_0$	Sample Size	1000

Parameters for Table 3.1			
Parameter	Value	Parameter	Value
Nominal maximum pressure rise $(\mu_{MPR})_0$	0.8	Mean throttle setting $E_{nom} = (\mu_E)_0$	2.9
Case F_6			
St. Dev. of maximum pressure rise $(\sigma_{MPR})_0$	$0.0050(\mu_{MPR})_0$	St. Dev. of inlet distortion amplitude $(\sigma_{ID})_0$	$0.0083(\mu_{MPR})_0$
Case F_7			
St. Dev. of maximum pressure rise $(\sigma_{MPR})_0$	$0.0037(\mu_{MPR})_0$	St. Dev. of inlet distortion amplitude $(\sigma_{ID})_0$	$0.0063(\mu_{MPR})_0$

Table C.4: Parameters used for generation of the figures and tables in Chapter 4

Parameters for Figure 4-2			
Parameter	Value	Parameter	Value
Nominal maximum pressure rise $(\mu_{MPR})_0$	0.8	Curve type	1033
St. Dev. of inlet distortion amplitude $(\sigma_{ID})_0$	$0.02(\mu_{MPR})_0$	Std. Dev. of tip clearance amplitude	1%

Parameters for Figures 4-3 and 4-4			
Parameter	Value	Parameter	Value
Nominal maximum pressure rise $(\mu_{MPR})_0$	0.8	Mean throttle setting $E_{nom} = (\mu_E)_0$	2.7
St. Dev. of inlet distortion amplitude $(\sigma_{ID})_0$	$0.02(\mu_{MPR})_0$	Std. Dev. of tip clearance amplitude	1%

Parameters for Figure 4-5			
Parameter	Value	Parameter	Value
Nominal maximum pressure rise $(\mu_{MPR})_0$	0.8	Curve type	1044
St. Dev. of inlet distortion amplitude $(\sigma_{ID})_0$	$0.02(\mu_{MPR})_0$	Std. Dev. of tip clearance amplitude	1%
Left plot: Mean throttle setting $E_{nom} = (\mu_E)_0$	2.8	Right plot: Mean throttle setting $E_{nom} = (\mu_E)_0$	2.75

Parameters for Figure 4-6			
Parameter	Value	Parameter	Value
Nominal maximum pressure rise $(\mu_{MPR})_0$	0.8	Curve type	1011
St. Dev. of inlet distortion amplitude $(\sigma_{ID})_0$	$0.04(\mu_{MPR})_0$	Std. Dev. of tip clearance amplitude	1%
Mean throttle setting $E_{nom} = (\mu_E)_0$	2.9		

Parameters for Table 4.1 and Figure 4-7			
Parameter	Value	Parameter	Value
Nominal maximum pressure rise $(\mu_{MPR})_0$	0.8	Curve type	1055
St. Dev. of inlet distortion amplitude $(\sigma_{ID})_0$	$0.005(\mu_{MPR})_0$	Std. Dev. of tip clearance amplitude	0.33%
Mean throttle setting $E_{nom} = (\mu_E)_0$	2.9		

Appendix D

Details of the Hynes-Greitzer Model

The algorithm of Hynes and Greitzer from [6] is used for compression system stability determination. The steady state mass flow distribution across the circumference is found from the combined compressor pressure rise and throttle equations:

$$\frac{p_5 - p_{t2}(\theta)}{\rho U^2} = \psi(\phi(\theta), \theta) - \lambda \frac{\partial \phi}{\partial \theta} - E(\frac{1}{2\pi} \int_0^{2\pi} \phi(\theta) d\theta)^2. \tag{D.1}$$

This equation is solved by a spectral collocation method which represents the mass-flow in Fourier series and allows efficient calculation of the differential and integral operators. The collocation points are uniformly distributed along the circumference and the resulting set of nonlinear equations is solved using the standard dogleg algorithm provided by `fsolve` in Matlab [23].

The coefficients λ and μ describing the fluid inertia are defined as:

$$\lambda = \frac{U}{r} \sum_{i=1}^{N} \tau_{R_i} \tag{D.2}$$

$$\mu = \frac{U}{r} \left[\sum_{i=1}^{N} (\tau_{R_i} + \tau_{S_i}) + \tau_{IGV} \right], \tag{D.3}$$

where U is the mean wheel speed, r is the mean wheel radius and the time constants

τ are defined as:

$$\tau = \frac{b_x}{U\cos^2\gamma}, \tag{D.4}$$

where b_x is the axial chord and γ is the stagger angle [6]. The subscripts S and R stand for stator and rotor, respectively.

Equation 4.1 gives rise to a small perturbation equation:

$$\frac{\delta p_4 - \delta p_{t2}}{\rho U^2} = \frac{\partial\psi}{\partial\phi}\delta\phi - \lambda\frac{\partial\delta\phi}{\partial\theta} - \frac{r\mu}{U}\frac{\partial\delta\phi}{\partial t}. \tag{D.5}$$

Assuming the following two spectral decompositions

$$\phi = \sum_{n=-\infty}^{\infty} a_n e^{in\theta + i\omega t} \tag{D.6}$$

$$\frac{\partial\psi}{\partial\phi} = \sum_{n=-\infty}^{\infty} c_n e^{i\omega\theta}, \tag{D.7}$$

a system of equations is obtained:

$$((\frac{2}{|n|} + \mu)\tilde{w} + \lambda n + ic_0)a_n = -i\sum_{s=-\infty,\, s\neq n}^{\infty} c_{n-s}a_s, \quad \text{for } n \neq 0 \tag{D.8}$$

$$(l_c\tilde{\omega} + ic_0)a_0 - i\delta\hat{p}_4 = -i\sum_{s=-\infty,\, s\neq 0}^{\infty} c_{-s}a_s, \quad \text{for } n = 0 \tag{D.9}$$

where ω is the frequency of the perturbation, $\tilde{\omega} = \frac{\omega r}{U}$ is the nondimentionalized frequency, n is the harmonic number, l_c is the nondimensional compressor length and $\delta\hat{p}_4 = \frac{\delta p}{\rho U^2}$ is the nondimensional plenum pressure perturbation. One additional equation can be obtained using mass conservation for the plenum volume

$$\left[4B^2 l_c i\tilde{\omega} + \frac{\pi}{E(\int_0^{2\pi}\phi(\theta)d\theta)}\right]\delta\hat{p}_4 = a_0, \tag{D.10}$$

where $B = \frac{U}{2a}\sqrt{\frac{V_{plenum}}{A_2 L_{tot}}}$ is Greitzer's parameter for the compression system, a is the speed of sound, V_{plenum} is the plenum volume, A_2 is the flow-through area and L_{tot} is the overall effective length of the compressor duct. Typically Equations D.9 and D.10 are combined into one equation eliminating $\delta\hat{p}_4$, but writing them separately allows

the use of efficient numerical eigenvalue algorithms. The numerical values of $\tilde{\omega}$ are obtained by truncating Equations D.8 and D.9, and solving them together with D.10 as an eigenvalue problem. The values of the model parameters are given in Table D.1 and correspond to the values for one of the experimental test compressors at MIT and were used by Graf in his asymmetric tip clearance investigation [1]. The values of c_n are determined from the compressor pressure rise characteristic using Fast Fourier Transform and the value of the integral in Equation D.10 comes from the steady state solution found earlier.

Table D.1: Hynes-Greitzer model parameters

Parameter	Value
B	0.05
λ	1.00
μ	1.01
l_c	$4 + \mu = 5.01$

Bibliography

[1] Graf, M. B., *Effects of Asymmetric Tip Clearance on Compressor Stability*, MS thesis, Massachusetts Institute of Technology, Department of Aeronautica and Astronautics, June 1996.

[2] Emmons, H. W., Pearson, C. E., and H.P.Grant, "Compressor Stall and Surge Propogation," *Transactions of ASME*, May 1955.

[3] Greitzer, E. M., "Surge and Rotating Stall in Axial Flow Compressors," *Journal of Engineering for Power*, Vol. 98, No. 2, April 1976, pp. 190–217.

[4] Moore, F. K., "A Theory of Rotating Stall of Multistage Axial Compressors," *Journal of Engineering for Gas Turbines and Power*, Vol. 106, April 1984, pp. 313–336.

[5] Moore, F. K. and Greitzer, E. M., "A theory of Post-Stall Transients in Axial Compression Systems," *Journal of Engineering for Gas Turbines and Power*, Vol. 106, Jan. 1986, pp. 69–76, 231–239.

[6] Hynes, T. P. and Greitzer, E. M., "A Method for Assessing Effects of Circumferential Flow Distortion on Compressor Stability," *Journal of Turbomachinery*, Vol. 109, No. 7, July 1987, pp. 371–379.

[7] Bonnaure, L. P., *Modelling High Speed Multistage Compressor Stability*, MS thesis, Massachusetts Institute of Technology, Department of Aeronautics and Astronautics, June 1991.

[8] Gordon, K. A., *Three Dimentional Rotating Stall Inception and effects of Rotating Tip Clearance Asymmetry in Axial Compressors*, PhD thesis, Massachusetts Institute of Technology, Department of Aeronautics and Astronautics, June 1999.

[9] van Schalkwyk, C. M., *Active COntrol of Rotating Stall with Inlet Distortion*, PhD thesis, Massachusetts Institute of Technology, Department of Aeronautics and Astronautics, June 1996.

[10] Haynes, J. M., Hendricks, G. J., and Epstein, A., "Active Stabilization of Rotating Stall in a Three-Stage Axial Compressor," *Journal of Turbomachinery*, Vol. 116, April 1994, pp. 226–239.

[11] Paduano, J. D., "Analysis of Compression System Dynamics," *Unpublished*, 2000.

[12] Garzon, V. E., *Probabilistic Aerothermal Design of Compressor Airfoils*, PhD thesis, Massachusetts Institute of Technology, Department of Aeronautics and Astronautics, Feb. 2003.

[13] Garzon, V. E. and Darmofal, D. L., "Impact of Geometric Variability on Axial Compressor Performance," *Journal of Turbomachinery*, Vol. 125, No. 4, Oct. 2003, pp. 692–703.

[14] Lavainne, J., *Sensitivity of Compressor Repeating-Stage to Geometric Variation*, MS thesis, Massachusetts Institute of Technology, Department of Aeronautics and Astronautics, Sept. 2003.

[15] Vincent, A., *Impact of Geometric Variability on Compressor Repeating-Stage Performance*, MS thesis, Massachusetts Institute of Technology, Department of Aeronautics and Astronautics, Sept. 2003.

[16] Srinivasan, R., *Importance Sampling*, Springer-Verlag, New York, 2002.

[17] Madras, N., *Lectures on Monte Carlo Methods*, Fields Institute Monographs, American Mathematical Society, Providence, Rhode Island, 2002.

[18] Smith Jr., L. H., "Casing Boundary Layers in Multistage Axial-Flow Compressors," *Flow Research on Blading*, edited by L. Dzung, Elsevier Publishing, Amsterdam, Netherlands, 1970, pp. 275–304.

[19] Graf, M. B., Wong, T. S., Greitzer, E., Marble, F. E., Tan, C. S., Shin, H. W., and Wisler, D. C., "Effects of Nonaxisymmetric Tip Clearance on Axial Compressor Performance and Stability," *Journal of Turbomachinery*, Vol. 120, No. 4, Oct. 1998, pp. 648–661.

[20] Richardson, J. H., Sallee, G. P., and Smakula, F. K., "Causes of High Pressure Compressor Deterioration in Service," *AIAA 79-1234*, 1979.

[21] James, A. D. and Weisel, D. R., "JT8D Engine Performance Retention," *NASA. Lewis Res. Center Aircraft Engine Diagnostics*, Jan. 1981, pp. 63–81.

[22] Steenken, W. G., "Engine Operability," *Aircraft Propulsion Systems Technology and Design*, edited by G. C. Oates, AIAA Education Series, chapter 6, American Institute of Aeronautics and Astronautics Inc., Washington, DC, 1989, pp. 337–382.

[23] The MathWorks Inc., *Optimization Toolbox User's Guide*, World Wide Web, `http://www.mathworks.com/access/helpdesk/help/toolbox/optim/`, Oct. 2004.